

Full 3D Modeling of Waveguide-Embedded Frequency Multiplier Arrays

Master's thesis in Microtechnology and nanoscience

GERGELY HRUBÓ

MASTER'S THESIS 2016

Full 3D Modeling of Waveguide-Embedded Frequency Multiplier Arrays

GERGELY HRUBÓ



CHALMERS
UNIVERSITY OF TECHNOLOGY

Terahertz and Millimetre Wave Laboratory
Department of Microtechnology and Nanoscience
CHALMERS UNIVERSITY OF TECHNOLOGY
Gothenburg, Sweden 2016

Full 3D Modeling of Waveguide-Embedded Frequency Multiplier Arrays

GERGELY HRUBÓ

© GERGELY HRUBÓ, 2016.

MCCX60 - Master's thesis in Microtechnology and nanoscience

Supervisor: Dr. Robin Dahlbäck, Terahertz and Millimetre Wave Laboratory

Examiner: Prof. Jan Stake, Terahertz and Millimetre Wave Laboratory

Master's Thesis 2016

Terahertz and Millimetre Wave Laboratory

Department of Microtechnology and Nanoscience

Chalmers University of Technology

SE-412 96 Gothenburg

Telephone +46 31 772 1000

Cover: Rendered image of the device modeled in a full 3D electromagnetic solver.

Typeset in L^AT_EX

Gothenburg, Sweden 2016

Abstract

The frequency region between 300 GHz - 10 THz has long been in interest of many scientific and industrial branches. However, the traditional ways to provide continuous wave (CW) signals are inapplicable at these frequencies due to fundamental limitations. There have been many approaches to bridge the lack of sources, commonly referred as the THz gap, both from the electronics and photonics side. To overcome the input power limitation of solid state electronics, quasi-optical grid arrays have been presented in order to spatially combine contributions from a large number of active devices. Originally they operate in free space environment, but to gain a compact component for i.e. satellite applications, the device can be enclosed in a waveguide. The interaction between the large number of nonlinear devices and the confined field in a waveguide cavity poses great modeling challenges.

The thesis is investigating different modeling techniques for waveguide embedded varactor frequency multiplier arrays. A Heterostructure Barrier Varactor (HBV) frequency tripler array operating at 250 GHz output frequency was experimentally tested and modeled with the traditional unit cell method and a novel approach using full 3D electromagnetic simulation. The full 3D model follows the abrupt changes of the measured results both as a function of frequency and input power due to the interaction between all the nonlinear elements. Furthermore, it enables the quantitative characterisation of individual diodes and provides knowledge of the total field distribution. In the evaluated example, higher order mode excitation was found due to the interaction between the filter and antenna array. An analysis to account for diode failures using the full 3D model is presented.

Due to the results obtained from the full 3D model, a new output filter was designed for the device. By matching the filter's periodicity to the antenna array, simulations show a decreased higher order mode excitation and therefore an increase of 1 dB in peak output power. RF measurements on the fabricated filter are reported, showing an increased output power at the lower edge of the measured band with a maximum increase of 0.8 dB at 243 GHz.

Altogether, the full 3D model provides a useful complementary to the present tools for waveguide-embedded grid array design. Taking into account the resource needs of the two models, the unit cell model is recommended for a quick design synthesis and the full 3D model can be employed for further improvements.

Keywords: Frequency Multipliers, Grid Array circuits, Heterostructure Barrier Varactors, Higher Order Modes, Spatial Power Combining, Terahertz Sources, Unit Cell Modeling.

Acknowledgements

I would like to express my deepest gratitude to my examiner, Prof. Jan Stake for giving me this opportunity, for always raising the proper questions and thus always setting the milestones to reach. I am greatly thankful to my supervisor, Dr. Robin Dahlbäck for guiding me to these milestones sparing no time and energy. His experience and persistence kept me going in times when there seemed to be no solution in sight.

There are many others who made this journey easier and more enjoyable for me. I would like to say thank to Dr. Peter Sobis for many fruitful discussions on simulation techniques, which taught me that doubtful questions diffuse and proliferate. Vladimir Drakinskiy kindly helped me processing my filter and Mats Myremark milled me waveguide shims within hours of notice. Two servers ran constantly to fulfill my model's computational needs, and Henric Fjellstedt took great care of these two. All the remaining staff of Terahertz and Millimetre Wave Laboratory deserves a thank for maintaining a friendly and fun working atmosphere.

Finally, I would like to thank my family and friends for their support and for dragging me out of the waveguides once in a while.

Gergely Hrubó, Gothenburg, June, 2016.

Contents

List of Abbreviations	xi
List of Notations	xiii
1 Introduction	1
1.1 Varactor frequency multipliers	1
1.2 Quasi-optical spatial power combining	1
1.3 Motivation of the thesis	2
1.4 Outline of the thesis	3
2 Theory	5
2.1 Heterostructure barrier varactor multipliers	5
2.1.1 The HBV diode	5
2.1.2 Symmetric varactor multipliers	7
2.2 Harmonic balance analysis	8
2.2.1 General overview	8
2.3 Linear 3D electromagnetic modeling	9
2.3.1 Boundary conditions and ports	10
2.3.2 Periodic boundary conditions	11
3 Methods	13
3.1 The device	13
3.2 Nonlinear model	14
3.3 Unit cell model	16
3.4 Full 3D model	17
4 Results	21
4.1 Model verification	21
4.2 Comparison of models	23
4.3 Failure analysis	28
5 New filter design and implementation	31
5.1 Design	31
5.2 Simulation results	31
5.2.1 S-parameter characterisation	31
5.2.2 RF characterisation	32
5.3 Fabrication	35

Contents

5.4	Measurements	37
5.4.1	VNA measurements	37
5.4.2	RF measurements	38
6	Conclusions and future work	41
	Bibliography	43

List of Abbreviations

AC	Alternating Current
BPF	Bandpass Filter
CV	Capacitance-Voltage
CW	Continuous Wave
DC	Direct Current
DFT	Discrete Fourier Transform
DLL	Dynamic Load Line
DUT	Device Under Test
EM	Electromagnetic
EMF	Electromagnetic Force
FEM	Finite Element Method
FSS	Frequency Selective Surface
GaN	Gallium Nitride
GHz	Gigahertz
HB	Harmonic Balance
HBV	Heterostructure Barrier Varactor
InGaAs	Indium Gallium Arsenide
InP	Indium Phosphide
IV	Current-Voltage
LO	Local Oscillator
RF	Radio Frequency
TE	Transversal Electric
THz	Terahertz
VBA	Visual Basic
VNA	Vector Network Analyzer

List of Notations

a	Empirical parameter
A	Device area
b	Barrier thickness
E_0	Empirical parameter
E_b	Electric field in the barrier
f_p	Pump frequency
I_{f3}	Steady state current at the third harmonic frequency
k	Boltzmann's constant
L_D	Debye length
N	Number of barriers
N_d	Doping concentration
P_{f3}	Steady state power at the third harmonic frequency
q	Elementary charge
R_s	Series Resistance
s	Spacer layer thickness
S_{max}	Maximum elastance
S_{min}	Minimum elastance
T	Junction temperature
$\tan\delta$	Dielectric loss tangent
V_{f3}	Steady state voltage at the third harmonic frequency
Z_C	Characteristic impedance
Z_L	Load impedance
Z_S	Source impedance
ϵ_b	Permittivity of the barrier
ϵ_d	Permittivity of the modulation layer
ϕ_b	Empirical parameter
σ	Electrical conductivity

1

Introduction

1.1 Varactor frequency multipliers

The frequency range between 300 GHz and 10 THz is denoted as the Terahertz (THz) region, and is considered to be the last unconquered part of the electromagnetic spectrum. Despite the demand it gets from space [1, 2], medical [3, 4], and security applications [5, 6], it still lacks high power coherent continuous wave (CW) sources which are essential as local oscillator (LO) signal in transmitters and heterodyne receivers. The traditional way to provide LO power in the microwave region (IMPATT, Gunn diodes, transistor oscillators) are inapplicable due to the transit time limitation in frequency. Thus, LO signals in the THz region rely on frequency up- or downconversion from the microwave and photonics frequency region, respectively.

Solid state frequency multipliers has proven to be the best option for signal generation around THz frequencies. Their compact size, long lifetime and low power consumption are the main motivation behind their application in the space industry. Depending on whether we use the intrinsic varistor or varactor of the active device, we differentiate between resistive and reactive frequency multipliers, respectively. Resistive multipliers can operate in a broad frequency range, but are limited to a $\frac{1}{n^2}$ theoretical efficiency limit [7, 8], where n is the multiplication factor. Reactive multipliers usually have a narrow bandwidth, but can reach a theoretical efficiency limit of 100%. For THz power generation, reactive multipliers are preferred and the workhorse devices are Schottky-diodes and Heterostructure Barrier Varactors (HBV) [9].

1.2 Quasi-optical spatial power combining

Solid state devices are limited in their maximum input power, therefore output of multiple devices has to be combined in order to fulfill the need for ever increasing output powers. Traditional waveguide power combiners are restricted to a number of several device ports as ohmic losses starts to play an increasing role as the number of combined ports grow. To overcome this, quasi-optical power combining was presented [10], where the transversal device sizes can exceed tens of wavelengths. The topic became hot in the late 20th century [11] and grid arrays have been presented for amplifiers [12, 13], oscillators [14, 15], and frequency multipliers [16, 17, 18] as well. As arbitrary number of elements can be placed in a grid array, there is no theoretical limit for the input power of quasi-optical systems. This comes handy for

those approaching the THz gap from the electronics side: thanks to the recent advancement in GaN Power Amplifier (PA) technology, the frequency multipliers can be pumped well above Watt level at W-band [19]. Such power levels are way over the limitations of conventional multipliers, and therefore the first step of a multiplier chain is an adequate role for a grid array frequency multiplier.

There have been a number of frequency multiplier arrays reported to operate in free space environment [18, 20, 21]. They typically use lenses to collimate the beams and gain a Gaussian field distribution. Because the beam is densely covered by the array, there is a small variation between the neighbouring devices and the unit cell approach holds fairly well. The biggest disadvantage of such array is being bulky, sensitive to alignment errors and thus not being feasible to be integrated in a system. To gain a compact component, one can implement the frequency multiplier array into a waveguide environment. It has the advantage that a guided wave environment provide: the field is confined and there is no chance for spatial spillage, thus to pump all the available input power to the diodes is just a matter of impedance matching. However, the price to pay for a confined field is a rapidly varying field distribution. This will cause high amplitude variations of the incoming field among diodes and considerable edge effects at the waveguide walls with field maxima, both of which imply as a challenge for modeling.

1.3 Motivation of the thesis

All the waveguide-embedded multiplier arrays that have been reported so far [16, 17, 22] have been designed using a unit cell approach. A single element of the grid is solved using a 3D electromagnetic solver technique (most commonly used are EMF and FEM), which is later coupled to a nonlinear model describing the device in use. This way the antenna and the matching impedances can be designed. By solving the unit cell in a 3D electromagnetic solver with periodic boundary conditions, the mutual coupling of the neighboring antennas can be implemented in the model.

There are many limitations of this approach. The finite number of elements can induce edge effects and the excitation is not a plane wave with normal incidence. These are limitations affecting every passive structure, but the main problems in a frequency multiplier array are caused by the presence of the large number of active devices. Because the quasi-impedance that a diode represents is input power dependent, the coupling between neighboring elements will be input power dependent as well. And because the array is excited by a fundamental waveguide mode, the quasi-impedance of the diodes and therefore the coupling between elements will be a function of the position across the array as well for a fixed input power. Moreover, the conversion efficiency of a diode is also input power dependent, which results in an uneven efficiency across the array and thus higher order mode excitation at the output frequency. Further limitations comes from the fact that the unit cell approach includes a single nonlinear model. This way it cannot account for diode yield occurring at processing (regardless of it being intentional or not) or device failures.

Computational capabilities has emerged to an extent which enables us to carry out a full 3D electromagnetic solver simulation of the entire device and couple it

to the total number of nonlinear elements in a circuit simulator. Such a model excludes the periodic boundary condition's assumption which restricts the accuracy of the passive structure, and include the effects of the numerous nonlinear devices. With less assumptions, a better prediction of the device performance is expected. Having all the nonlinear elements present is also attractive for the sake of gaining knowledge of their voltages and currents. This opens up new possibilities in device characterisation.

1.4 Outline of the thesis

The thesis starts with a brief description of the background of Heterostructure Barrier Varactors, frequency multipliers, nonlinear device modeling and computational electromagnetics. Chapter 3 then presents the implementation of the unit cell model and the full 3D model. Chapter 4 compares the results and capabilities of the two models. Chapter 5 described the realisation of a new filter for the device from design to measurement, which was motivated based on the results obtained in Chapter 4. Conclusion and future possibilities are discussed in Chapter 6.

2

Theory

2.1 Heterostructure barrier varactor multipliers

2.1.1 The HBV diode

The Heterostructure Barrier Varactor was first presented in 1989 [23]. It consists of an undoped, high bandgap barrier layer sandwiched between the modulation layers. The ability to stack several layers on top of each other highly increases the power handling capability of the diode. On the other hand, due to the low thermal conductivity of the modulation layer, the increasing number of barrier layers induce more heat which has to be treated carefully [24]. Therefore, there is an optimum number of barrier layers to be chosen based on the incident power level per device area. An HBV equivalent model can be seen in Fig. 2.1.

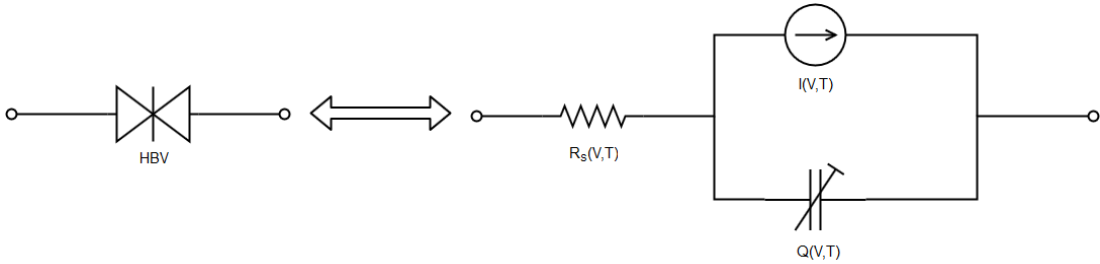


Figure 2.1: Equivalent circuit model of the HBV.

Due to the symmetric geometry of the diode it presents an anti-symmetric IV and symmetric CV diagram (shown in Fig. 2.2) and therefore only odd harmonics are generated. This allows us to exclude idler circuits designated to reflect even harmonics, and a tripler can be designed without the need of any idler circuit. The symmetric CV curve also provides the single biggest advantage of the HBV which is that no bias is required for operation.

The voltage-charge relationship is best explained by a fifth-order polynomial model [25]:

$$V(Q) = N \left(\frac{bQ}{\epsilon_b A} + 2 \frac{sQ}{\epsilon_d A} + \text{sign}(Q) \left(\frac{Q^2}{2qN_d \epsilon_d A^2} + \frac{4kT}{q} \left(1 - e^{-\frac{|Q|}{2L_D A q N_d}} \right) \right) \right) \quad (2.1)$$

The conduction current of the diode is described by an empirical equation [25]:

$$J = AaT^2 \sinh \left(\frac{E_b}{E_0} \right) e^{-\frac{\phi_b}{kT}} \quad (2.2)$$

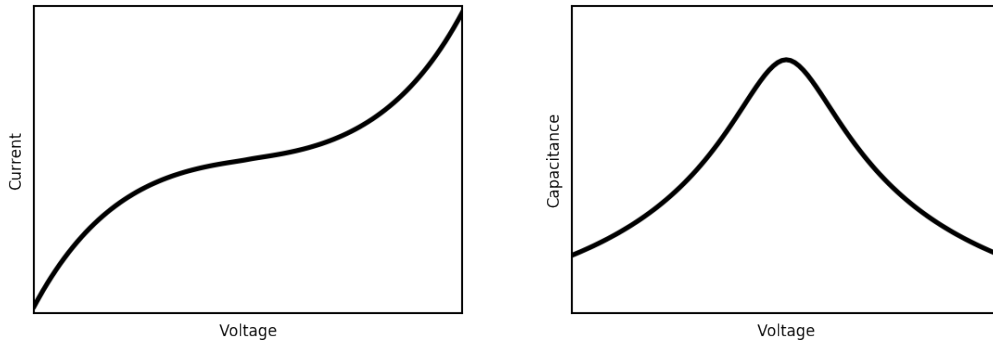


Figure 2.2: Typical IV and CV curves of an HVB.

where a , E_0 and ϕ_b are empirical constants, T is the temperature, A is the device area and E_b is the electric field in the barrier described by

$$E_b = \frac{N_d q \epsilon_d b}{\epsilon_b^2} \left(\sqrt{1 + \frac{2V \epsilon_b^2}{N_d q \epsilon_d b^2 N}} - 1 \right) \quad (2.3)$$

where V is the voltage of the diode.

The series resistance is an important and inevitable parameter of the device which degrades the overall performance. The power dissipated by it is equivalent to dissipated heat in the device which provides a positive feedback through the increase in conduction current. It consists of contributions from different parts of the diode geometry, such as [26]:

$$R_s(T) = R_c + R_{active}(T) + R_{contact}(T) + R_{spread}(T) \quad (2.4)$$

where R_c is the contact resistance and $R_{active}(T)$, $R_{contact}(T)$, and $R_{spread}(T)$ are the resistance of the active, contact, and buffer layer, respectively. Extracting the series resistance of an HBV is a more challenging task compared to the other parameters. Usually a good first iteration step is to calculate the resistances of the different layers with

$$R = \frac{t}{A\sigma} \quad (2.5)$$

where A is the device area, t is the layer thickness and σ is the conductivity of the layer. Later the series resistance can be fine tuned from measured data as the slope of the power sweep curve of a frequency multiplier for low input powers is mostly dominated by R_s .

An important figure of merit of varactors operating at high frequencies is the dynamic cutoff frequency [27] which is defined as:

$$f_c = \frac{S_{max} - S_{min}}{2\pi R_s} \quad (2.6)$$

where S_{max} and S_{min} are the maximum and minimum elastance, respectively. Fig. 2.3. shows how the theoretical efficiency limit is related to the cutoff frequency [28, 29, 30]. Therefore it is imperative to keep the series resistance as low as possible. HBV material systems usually have bad thermal conductivity and given the multiple stacked layers we can state that the bad thermal behaviour is a drawback of HBVs.

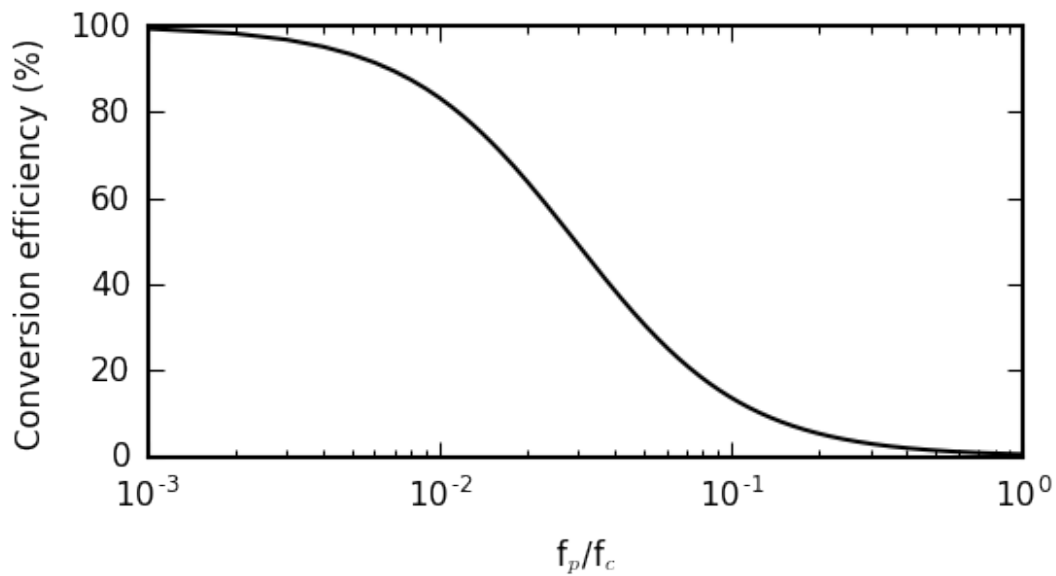


Figure 2.3: Theoretical limit for efficiency as a function of cutoff frequency.

2.1.2 Symmetric varactor multipliers

Fig. 2.4 shows the schematic of a single diode frequency multiplier. The output bandpass filter (BPF) is responsible for blocking the fundamental frequency to leak into the load and maximise the delivered power to the diode. The input BPF is responsible to prevent the leakage of the output frequency to the generator. The matching networks are responsible for presenting the adequate embedding impedances for the diode. The optimum embedding impedances for maximum efficiency can be described by empirical expressions described in [29]. Quasi-optical multipliers has the same working principle as single diode multipliers. The only exception is that the input BPF can be absent since it was shown that for substrates with similar dielectric constants only 2% of the radiated power propagates to the direction of air from an antenna array[31, 32].

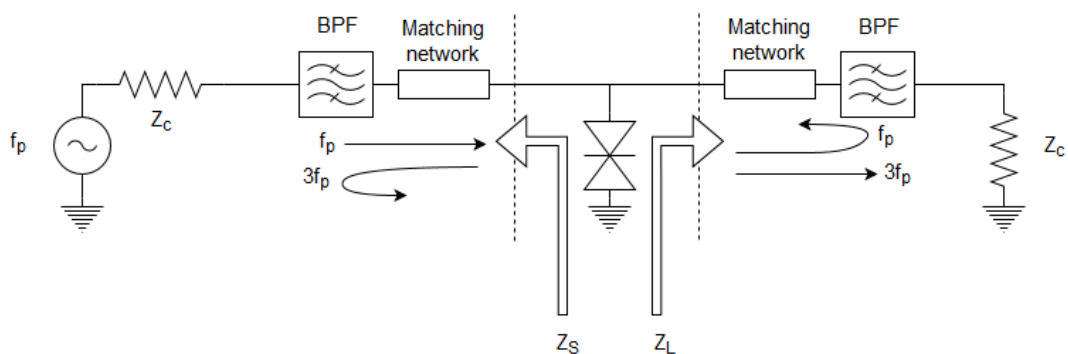


Figure 2.4: Conceptual schematic of a single diode frequency multiplier.

2.2 Harmonic balance analysis

2.2.1 General overview

Harmonic Balance (HB) is the most popular technique to analyze nonlinear RF and microwave circuits, mainly because its robustness. It is applicable to circuits with a large number of nonlinear elements with different time constants, a scenario which is otherwise very time consuming to solve with time domain methods. Its theory is well covered in [33], which will be briefly introduced here.

HB first divides the circuit into linear and nonlinear part as depicted in Fig 2.5. The goal of the technique is to find a $V_i(f)$ for $i = 1, 2, \dots, N$ and $f = 0, f_0, 2 * f_0, \dots, K * f_0$ which satisfies $I_{NLi}(f) = I_{Li}(f)$ for every i and f , where f_0 is the frequency of our single tone excitation. To achieve this, an initial guess is required for the voltages. The merit on which we judge our solution is called the current-error vector.

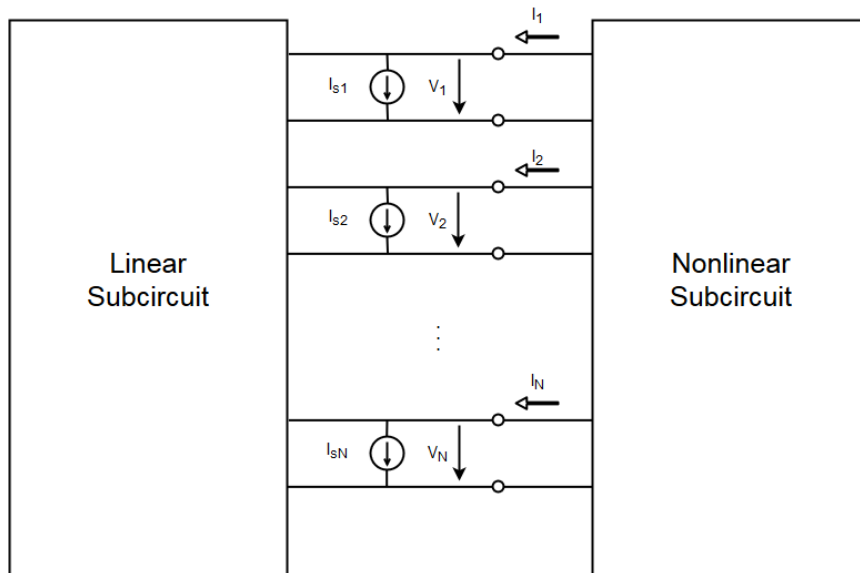


Figure 2.5: Conceptual schematic of the Harmonic Balance technique.

The Harmonic Balance Equation for a network with N nonlinear elements, P ports and K frequencies to be taken into account:

$$\mathbf{F}(\mathbf{V}) = \mathbf{I}_s + \mathbf{Y}_{N \times N} \mathbf{V} + jkw\mathbf{Q} + \mathbf{I}_G = \mathbf{0} \quad (2.7)$$

where

- \mathbf{I}_s is the current at each port transformed by the linear subcircuit $(N+P) \times (N+P)$ admittance matrix from the source ports.
- $\mathbf{Y}_{N \times N}$ is the admittance matrix of the linear subcircuit.
- \mathbf{V} is the voltage at each port.
- \mathbf{Q} is the charge stored at each port as in nonlinear capacitors.
- \mathbf{I}_G is the current in a controlled current source..

Each element of $\mathbf{Y}_{N \times N}$ is a $(K+1) \times (K+1)$ diagonal matrix, consisting of the values of $\mathbf{Y}_{N \times N}$ for DC and the K^{th} harmonic. Each element of \mathbf{I}_s , \mathbf{V} , \mathbf{Q} , and \mathbf{I}_G is

a $(K+1) \times 1$ subvector, consisting of the values of \mathbf{I}_s , \mathbf{V} , \mathbf{Q} , and \mathbf{I}_G respectively for DC and the K^{th} harmonic.

It is important to state that despite the currents are compared in their frequency domain form, it is being solved in time-domain for the nonlinear elements, relying on their CV and IV characteristics. The transition between the frequency and time domain is provided by the Fourier transformation. The port currents of the linear subcircuit are determined simply by the admittance matrix of the subcircuit from the node voltages.

To solve the Harmonic Balance equation, almost every circuit simulator nowadays uses the Newton-Raphson method. It relies on all the derivatives of a multivariable function and hence very powerful. On the other hand, it depends on very much on the initial guess. It is important that nonlinear circuits (and especially circuits with huge number of nonlinear devices) can end up in different solution stages. The Newton-Raphson method can easily get stuck in local minimas, ending up showing a false solution.

The scope of this thesis is to deal with large number of nonlinear elements under single tone excitation. As our HBVs are InGaAs/InAlAs on InP substrate, the conduction current is greatly reduced [34]. Therefore the CV characteristics will play a much dominant role. The volume of the linear electromagnetic environment is linearly increasing with frequency and therefore solutions cannot be obtained for higher tones. On the other hand, the accuracy of the HB method highly depends on the number of higher harmonics included. To compromise, the higher harmonics included to increase the accuracy has to be taken care of a different way, which will be described in Sec. 3.2.

2.3 Linear 3D electromagnetic modeling

The linear part of our Harmonic Balance simulation is an S-parameter representation of the geometry. There exist many computational techniques to solve the electromagnetic field in a media, the most common ones are: Finite Element Method (FEM), Finite Difference Time Domain (FDTD), Method of Moments (MoM). The commercial software Ansys HFSS used in this thesis is based on the FEM technique.

For obtaining the steady-state response of highly resonance structures FEM [35] is the method of choice. It is used to solve differential equations, which has a general form of:

$$L[f(\vec{r})] = s(\vec{r}) \quad (2.8)$$

where s is the source, L is the differential operator and f is the field distribution we wish to obtain. The method starts with dividing the geometry into finite subdomains (meshing) of either hexahedron or tetrahedron. The subdomains fill the entire geometry and do not overlap with each other. The FEM then applies a basis function at each subdomain through which an approximated field distribution will be known. The most common basis function is a tent function, which is $\phi_i(\vec{r}) = 1$ at node i and $\phi_i(\vec{r}) = 0$ at every other node. We assign a set of coefficients f_i to the corresponding basis functions, which represents the discrete approximation of the

continuous function $f(\vec{r})$.

$$f(\vec{r}) = \sum_{n=1}^N f_n \phi_n(\vec{r}) \quad (2.9)$$

The goal of the solver is to minimize the residual error $r(\vec{r}) = L[f(\vec{r})] - s(\vec{r})$ weighted with some function $w_i(\vec{r})$. The weighting function $w_i(\vec{r})$ usually equals the basis function $\phi_i(\vec{r})$ (Galerkin's method).

2.3.1 Boundary conditions and ports

When carrying out FEM simulation, at the edge of the computational domain one needs to describe the behaviour of $f(\vec{r})$. It is possible to either set fixed values at the boundary ($f(\vec{r}) = f_0(\vec{r})$, Dirichlet boundary condition) or to define the normal derivative of the field on the surface ($\frac{\partial f(\vec{r})}{\partial \vec{n}} = f_0(\vec{r})$, Neumann boundary condition). To have a unique solution, at least one Dirichlet boundary condition is necessary.

In the following we will discuss only the theory behind simulating electromagnetic fields in a guided wave environment. HFSS also enables us to simulate free space propagation and thus gain knowledge of radiation patterns of antennas, but that is beyond the scope of this thesis.

In a waveguide environment the boundary conditions are generally some finite conductivity. The following relations hold for the electric and magnetic field:

$$\vec{E}_t = \frac{1}{\sigma_s} (\hat{n} \times \vec{H}_t) \quad (2.10)$$

where \vec{E}_t and \vec{H}_t are the transversal electric and magnetic fields respectively, \hat{n} is the normal of the surface and σ_s is the surface conductivity. By default HFSS treats every surface as Perfect Electric Conductor (PEC) with $\sigma_s \rightarrow \infty$ thus $\vec{E}_t = 0$. It is important to note that the finite conductivity is directly related to the attenuation coefficient in transmission line theory. Having a transverse component appearing on a conductor's surface equals heat being dissipated. From a computational point of view the transverse component has a negative feedback for the propagating fields.

In order to couple energy into the system, wave ports are used. They must be defined on the border of our computational domain and can only very seldom be placed inside. Wave ports has two roles: after their natural field distributions (modes) are being calculated, they serve as a Dirichlet boundary condition. Besides this, they also serve as a number of Perfectly Matched Layer (PML) to provide a reflectionless interface when simulating S-parameters. HFSS assumes that the wave ports extend semi-infinitely having the same cross-section and material properties. It automatically assigns propagation constant and characteristic impedance to every propagating mode. When HFSS measures the incoming wave at a wave port during S-parameters simulation, it also assumes that the incident field is a set of propagating modes. Therefore it is essential to place the wave port far enough from any kind of discontinuity in order to allow evanescent modes to decay. The deembedding function is useful to gain knowledge of the S-parameters at a reference plane close to discontinuities.

Sometimes it can be essential to measure S-parameters at an interface inside our computational domain. In such cases lumped ports are used. These no longer use

the assumption of semi-infinite waveguides and therefore a complex port impedance has to be assigned to them. It is advised to place the lumped ports to places where the field distribution would be the same in the absence of the lumped port as the lumped port's fundamental mode. Typical example is a lumped port between conductors which later in a circuit simulator can be used for tuning with lumped capacitance or adding the nonlinear component.

2.3.2 Periodic boundary conditions

HFSS is prepared to work with infinite arrays. It enables us to simulate one unit cell of an infinite array and assign periodic boundary conditions with Floquet port excitation, named after Floquet's theorem [36]. Periodic boundary conditions consist of Master and Slave boundary pairs, which must be a planar surface with an identical geometry. Furthermore, HFSS forces the electric field on the Slave boundary to have the same magnitude and a phase difference as the corresponding point on the Master boundary. Floquet ports are the interface used to couple in energy when working with planar periodic arrays. It requires Master and Slave boundary conditions defined at its boundaries and represents a semi-infinite space to the outwards direction. It is very similar to the wave port in a sense that the field is described by a set of modes, to which a propagation constant and a cutoff frequency is assigned. The fundamental mode is a plane wave, whose propagation constant is frequency independent (no cutoff frequency). These tools altogether are useful to analyse antenna arrays and frequency selective surfaces (FSS). However, they should be treated carefully. Practical devices are never infinite in size and this result in the variation of the electric field across the array. Generally, the accuracy of this modeling technique is highly dependent on how densely the array is covered with respect to the electric field variation. Smaller amplitude variation in a single unit cell leads to more accurate results.

3

Methods

The body of the thesis is comparing two methods to model a waveguide-embedded frequency multiplier array: a full 3D model which solves the entire geometry of the device with waveguide boundary conditions, and a unit cell model which solves one unit cell of both the multiplier and filter array.

3.1 The device

The device to model is a waveguide embedded frequency tripler array, which was originally presented in [17]. The core of the device is a 6x12 InGaAs/InAlAs HBV grid coupled to bowtie antennas on a 185 μm thick InP substrate. The HBVs are utilising a double-mesa construction with 6 barriers in total and a device area of 20 μm^2 , with the same material structure as the one used in [37]. The output filter fabricated on a 150 μm thick Quartz substrate and is located on the other side of the InP substrate. The input matching network is a 380 μm thick InP substrate, and the input filter is absent due to reasons mentioned in Sec. 2.1.2. The output of the multiplier array's waveguide shim is connected to a linear taper which provides a smooth transition from WR10 to WR3 waveguide size in order to ensure a single mode output.

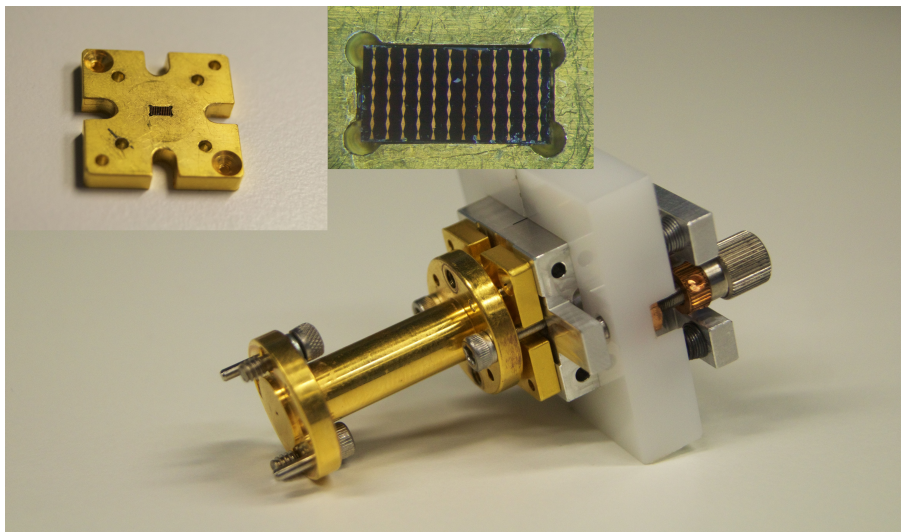


Figure 3.1: Photograph of the modeled device. Top left is a photograph of the multiplier array housing shim separately and top middle is a photograph of the mounted multiplier array.

The measurement setup used to characterise the device is shown in Fig. 3.2. The input signal is provided by a frequency synthesizer and a frequency multiplier chain having a x12 overall multiplication factor. The coupler located before the DUT enables us to measure input power and reflected power as well. The swept frequency band was limited by the S22 and isolation bandwidth of the circulator. Big reflection affects the measured input power resulting in a big uncertainty, and poor isolation can damage the Power Amplifier (PA). The swept input power was limited by the saturation of the PA. At the output of the DUT a WR3-WR10 linear taper widens back the waveguide to WR10 size of the power meter. The 3 power meters, the programmable attenuator and the frequency synthesizer are connected through General Purpose Interface Bus (GPIB) cables and are programmed using a Python script.

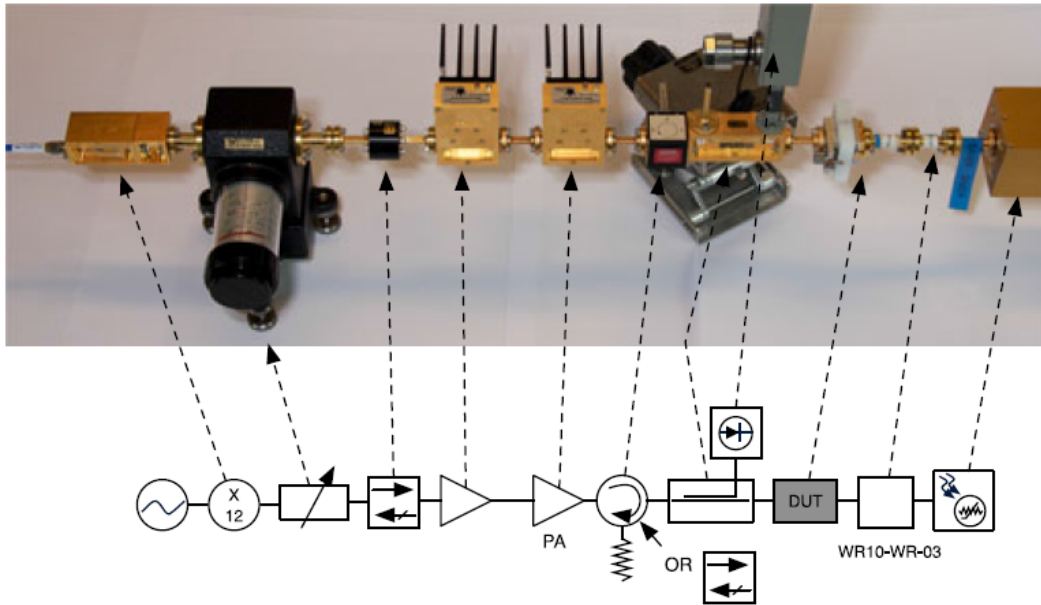


Figure 3.2: Picture and schematic showing the RF measurement setup [17].

3.2 Nonlinear model

The HBV model described in Section 2.1 was used in both models, it was already implemented in NI Microwave Office [38]. Variables a , E_0 and ϕ_b were used to fit the diode model IV curve to the measured IV curve. The capacitance model was extracted by applying a small signal AC voltage to the diode while sweeping the bias voltage. From Fig. 2.1 the capacitance can be extracted as

$$C = -\frac{1}{2\pi f \operatorname{Im}\left(\frac{v_d}{i_d}\right)} \quad (3.1)$$

where v_d and i_d are the diode voltage and current respectively and f is the frequency. This is done under the assumption that the displacement current is much higher than

the conduction current. Data obtained from NI Microwave Office shows that there is 5 order of magnitudes difference between them. The fitted curves with the measured ones are depicted in Fig. 3.3.

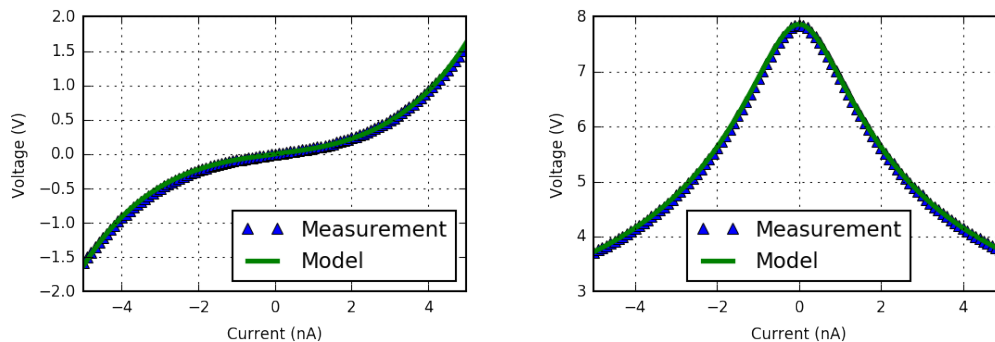


Figure 3.3: IV and CV curves of the diode model and measured data.

In Fig 3.4 the diode model is shown supplemented by additional circuit elements, which is placed to the designated lumped ports in both models. The voltage and current meters are used to gain quantitative details about the diode currents and voltages in the models. The parallel resistance $R(f)$ has the following values:

$$R(f) = \begin{cases} 10^{-6}, & f < f_p \\ 10^{12}, & f_p \leq f \leq 3f_p \\ 10^{-6}, & 4f_p \leq f \end{cases} \quad (3.2)$$

where f_p is the pump frequency. This resistance is placed there in order to present a parallel short circuit at DC and harmonics above the third. The purpose of this is to prevent false results due to extrapolation of the S-parameters, because solutions of the full 3D linear model were not obtained for these frequencies.

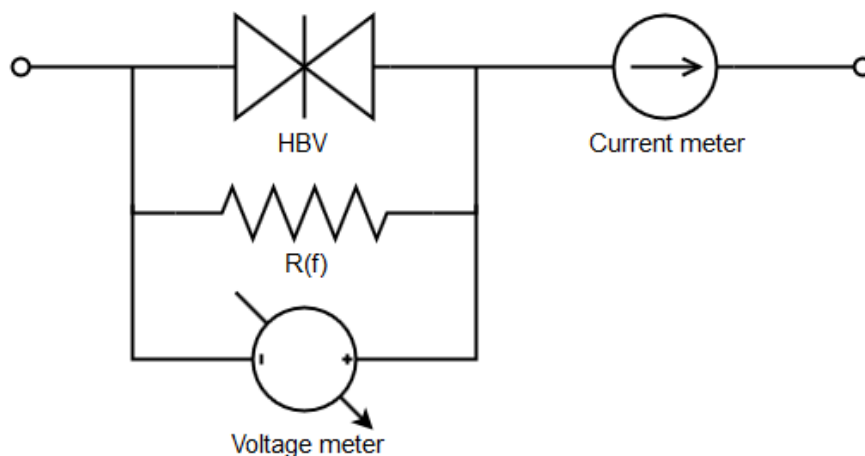


Figure 3.4: The nonlinear diode model used in both the unit cell and full 3D model's harmonic balance simulation. The HBV model is supplemented by additional circuit elements for quantitative characterisation and HB simulation control.

In the following sections the term 'diode model' will be referring to Fig. 3.4.

3.3 Unit cell model

The unit cell model [39] relies on the periodic boundary conditions technique described in Sec. 2.3.2. Both the multiplier array and the FSS are assumed as infinite arrays in the linear simulation. A conductivity of $\sigma = 2 * 10^7 \frac{S}{m}$ was assigned to the metal parts. This is intentionally lower than the gold conductivity in order to account for surface roughness. The dielectrics were simulated lossy with $\tan\delta = 0.001$ for Quartz and $\tan\delta = 0.002$ for InP. The resulting S-parameters, together with the matching slab's and taper's S-parameters are then cascaded in NI Microwave Office. The diode model is then coupled to the unit cell S-parameters of the multiplier array to perform the Harmonic Balance simulation.

This method has been further developed [17] by simulating multiple cascaded unit cell models with different input powers. This is ought to account for the input power level variation among the multiplier. Since we assume that the fundamental mode electrical symmetry is not violated, and the diodes in the same column receive the same input power, we only need to simulate 6 cascaded lines this way. These 6 lines are excited with a \sin^2 input power variation among them, defined as:

$$P_n = \frac{P_{tot} S_n}{m S_\pi} \quad (3.3)$$

where P_{tot} is the total input power, m is the number of rows, n is the number of the current column and the S_n/S_π ratio denotes the relative power density in a unit cell in column n . In order to account for the phase difference between the output power contribution from different unit cells, the output powers are combined with an ideal power combiner described by the following S-parameters:

$$S = \begin{bmatrix} 0 & t & t & t & t & t & t \\ t & 0 & 0 & 0 & 0 & 0 & 0 \\ t & 0 & 0 & 0 & 0 & 0 & 0 \\ t & 0 & 0 & 0 & 0 & 0 & 0 \\ t & 0 & 0 & 0 & 0 & 0 & 0 \\ t & 0 & 0 & 0 & 0 & 0 & 0 \\ t & 0 & 0 & 0 & 0 & 0 & 0 \end{bmatrix} \quad (3.4)$$

where $t = \frac{1}{\sqrt{6}}$. The input matching slab and the linear taper at the output present the same S-parameters as in the full 3D model. Figure 3.5 shows the schematic of the unit cell model.

Our unit cell method is based on the following assumptions:

1. The input power distribution matches the TE_{10} mode.
2. The output power only excites the TE_{10} mode.
3. There is no phase difference in the contribution of each diode to the output power due to the linear electromagnetic environment.
4. The antenna array is infinite (no edge effect) and receives a plane wave.
5. The TE_{10} electrical symmetry has not been violated.

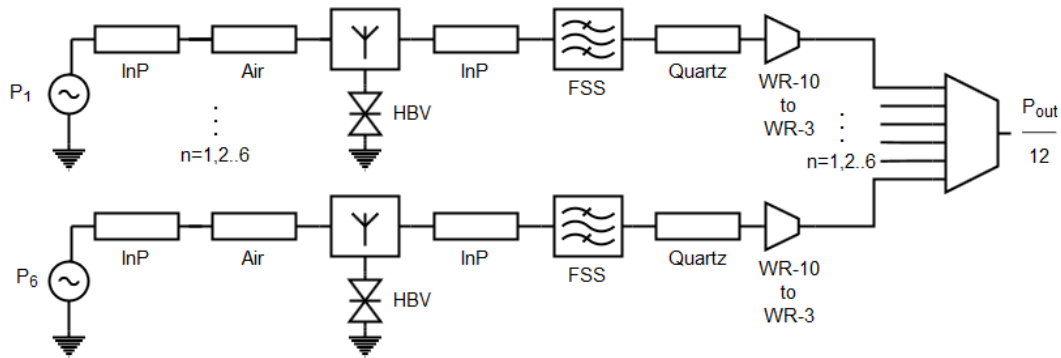


Figure 3.5: Schematic of the unit cell model. Six sets of equal unit cell chains are applied, each representing one of the six array columns modeled. The unit cell chains are excited by power corresponding to their position in the waveguide and the output is vectorially combined using ideal power combiners.

3.4 Full 3D model

The concept of the full 3D model is to solve the field distribution in the entire geometry using FEM technique and present every diode in a Harmonic Balance analysis. There are many ways the assumptions of the unit cell method can fail, and a model which is in knowledge of the field distribution over the entire geometry is a good way to verify these assumptions. Most likely sources of error are the waveguide boundary conditions, the finite area of the array, interaction between the multiplier array and filter, coupling between the nonlinear elements excited with different input powers in the multiplier array, and the properties of spatial power combining which is far from ideal power combiners.

In the full 3D model, the waveguide boundary conditions and the metal parts use the same finite conductivity as in the unit cell model, as well as the dielectrics have the same $\tan\delta$. The mounting pockets are not included because the model should correspond to 6x12 unit cells in order to gain knowledge of the effects listed above. An initial mesh operation was set in the dielectrics by restricting the maximum length of elements. This is to ensure that an essential amount of subdomains are present in these electrically large volumes, where most of the fields are confined. It also increases the speed of the solver because from a poor initial mesh it would take several iteration steps to reach this user defined mesh setup. It is essential to include all the propagating modes at the input port, otherwise HFSS represents a short circuit to them. This short circuit causes standing waves between the device and the port which corrupts the S-parameter results. A lumped port is placed at each bowtie antenna to provide a port for the diode model in the harmonic balance simulation. Thus, the linear part of the harmonic balance simulation is a $(N+M+K) \times (N+M+K)$ matrix, where N is the number of lumped ports, representing one diode each, M is the number of waveguide modes solved at the input port, K is the number of waveguide modes included at the output port. The convergence criteria for the higher order modes at the input was manually turned off when simulating the fundamental frequency, because those modes do not propagate at that frequency. A rendered image of the linear part of the full 3D model is shown

in Fig. 3.6.

In this example the number of diodes in the device is $N=72$, all the $M=14$ propagating modes have been included in the input, and due to the linear taper we have a single mode operation at the output therefore $K=1$. In NI Microwave Office a diode model presented in Sec. 3.2. is placed to each of the lumped ports. Every port representing a waveguide mode is terminated with its corresponding characteristic impedance. The fundamental mode at the input is excited with the total input power. A schematic of the full 3D model is shown in Fig. 3.7, and a picture of how it is implemented in a circuit simulator is shown in 3.8.

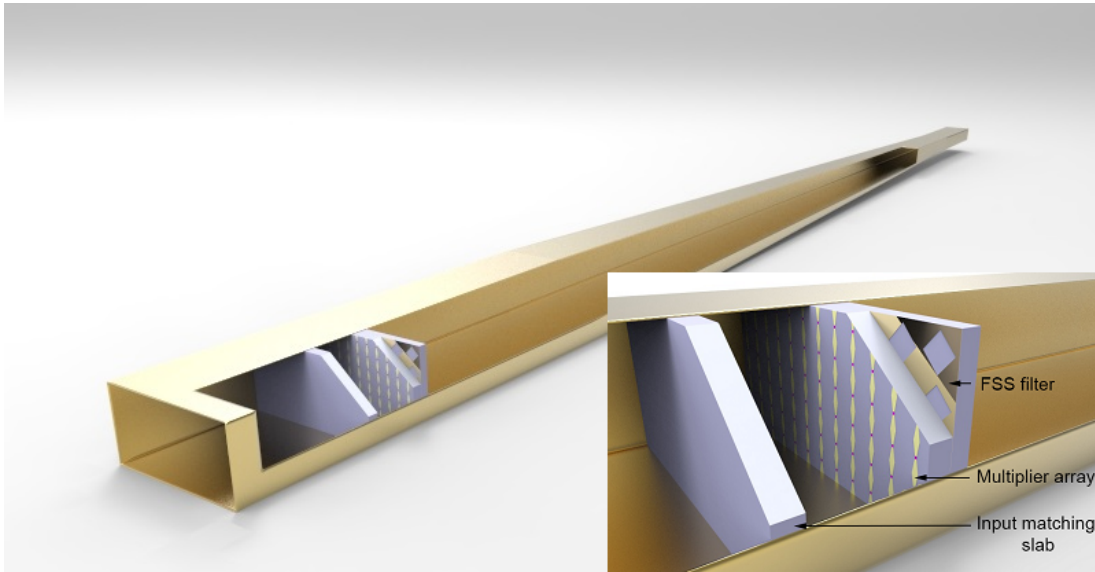


Figure 3.6: Rendered image of the linear part of the full 3D model implemented in HFSS. The bottom right corner shows a magnification of part of the model.

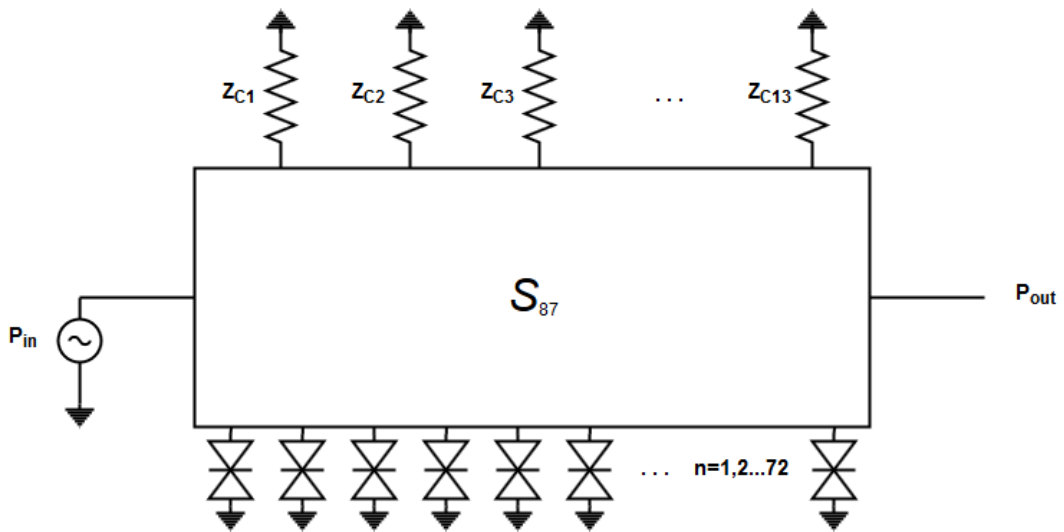


Figure 3.7: Schematic of the full 3D model. Z_{C_i} denotes the characteristic impedance of the higher order modes.

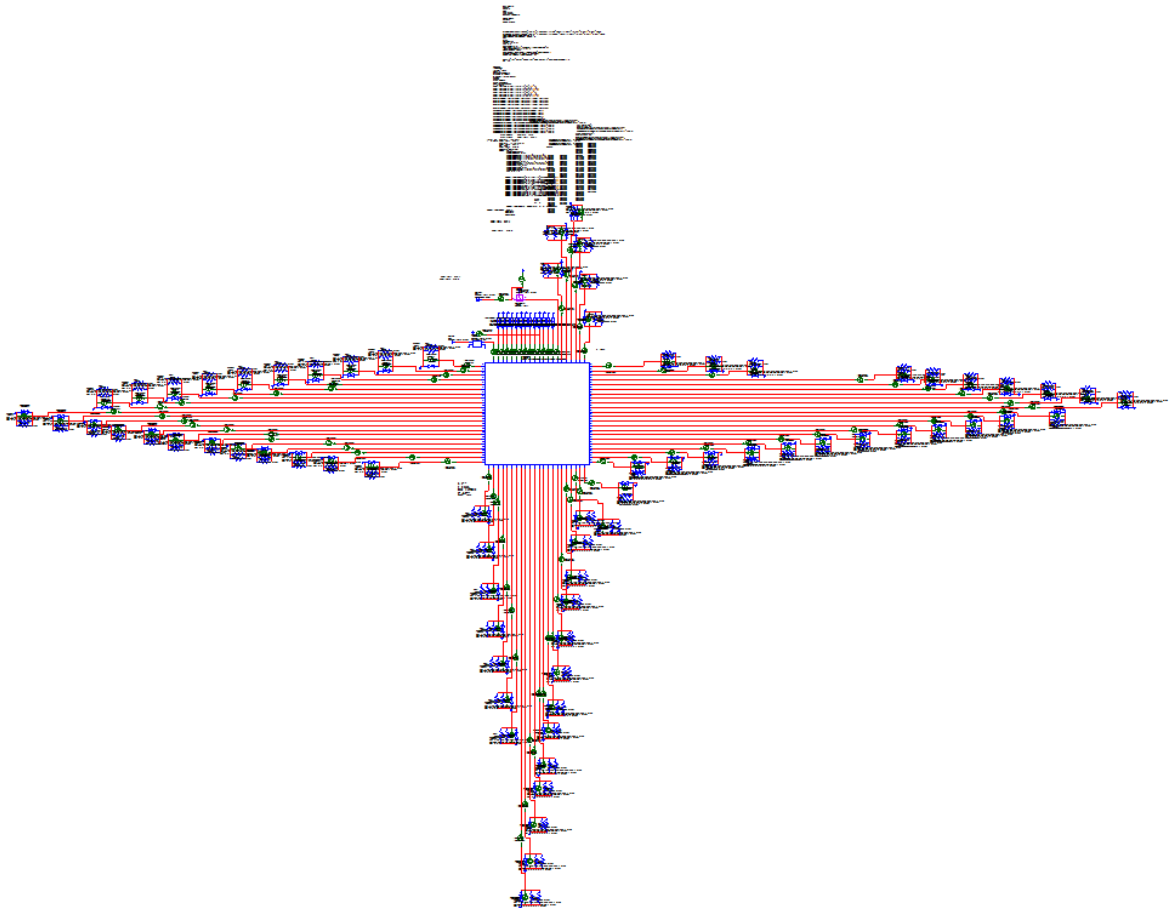


Figure 3.8: Harmonic Balance simulation of the full 3D model implemented in NI Microwave Office. The box represents the 87-port S-parameter file, connected to 72 diode models, to impedances terminating higher order modes and to the input and output port.

4

Results

4.1 Model verification

The models are verified with RF measurements carried out on an HBV-based waveguide-embedded frequency tripler array, described in Sec. 3.1. The output power was measured as a function of input power at an output frequency of 247 GHz and as a function of frequency for an input power of 300 mW. The output frequency for the power sweep was chosen to be the frequency for which the array is matched. The input power level for the frequency sweep was chosen to be high enough in order to allow the majority of the diodes to work at saturated efficiency, but low enough to avoid significant thermal feedback. Fig. 4.1. and Fig. 4.2. shows the output power of the two models and three different measurement runs of the same device after reassembling versus frequency and input power, respectively. Return loss is also plotted in Fig. 4.1. The shaded area indicates measurement uncertainty of the power meter for the measurement denoted by blue circles. 2 dB loss was added to the models to account for additional loss mechanisms that are not included in the models:

- The unknown diode yield. Both models utilise the same nonlinear model across the array. However, we performed DC measurements on each and every diode and found 3 orders of magnitude difference in conduction current. The conduction current does not play a role in the device's RF performance, but this is a good indication of the non-perfect diode yield.
- The input matching network is housed in a separate waveguide shim, which enables us to carry out S-parameter measurements on it and implement an equivalent slab in the models. However, in reality the slab is slightly tilted and do not fill the waveguide perfectly, which results in a perturbation in the embedding impedance across the array.
- The manual assembly of the device causes an uncertainty in transversal alignment of the grid array and filter. This is also the most likely cause of the difference between measurement runs, which can reach up to 2 dB as shown in Fig. 4.1.
- The array substrate is likely to have some surface conductivity which is originating from the imperfect removal of the seed layer used for gold plating.

The full 3D model follows the measured output power versus input power curve accurately at the design frequency. However, the different slope in the frequency sweep causes an increasing discrepancy between the full 3D model and measurement data as the frequency changes. A possible origin of this is the non-perfect diode yield,

which narrows down the operation band. Altogether, the full 3D model catches the trend of the measured output power both as a function of input power and frequency. The unit cell model agrees with the full 3D model for low output powers, however it fails to follow the abrupt changes of the measured curves and thus peaks at a 2% shifted frequency. This is most likely due to the absence of the coupling between the many nonlinear elements. The lower peak output power of the unit cell method is due to the even phase transmission of the ideal power combiners, which differs in spatial power combining.

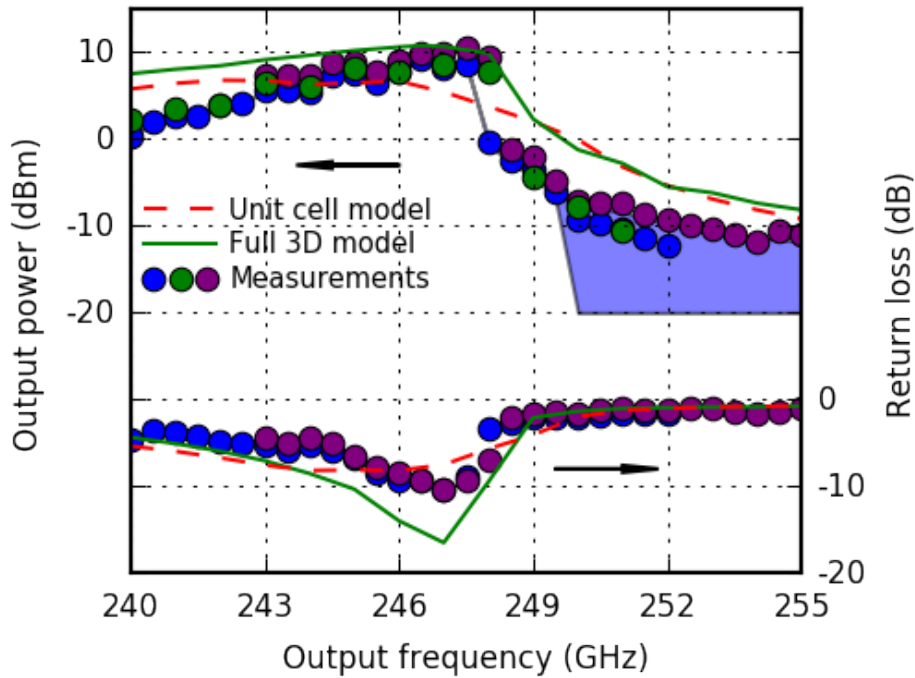


Figure 4.1: Output power of the measured frequency multiplier array, the full 3D model and the unit cell model as a function of output frequency for input power of 300 mW. Measurement uncertainty of the power meter for the measurement run shown with blue circles is indicated with the shaded region.

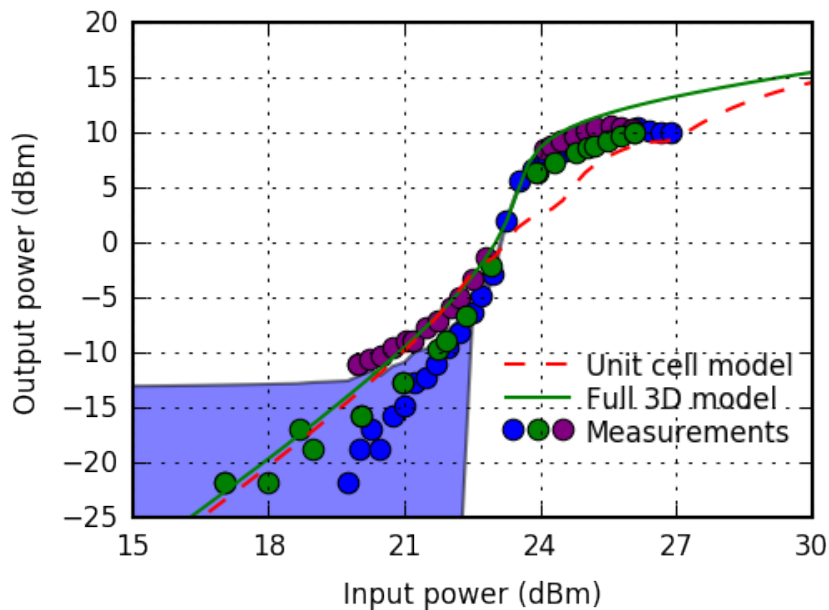


Figure 4.2: Output power as a function of input power for the measured frequency multiplier array, the full 3D model and the unit cell model at 247 GHz output frequency. Measurement uncertainty of the power meter for the measurement run shown with blue circles is indicated with the shaded region.

4.2 Comparison of models

The biggest advantage of the full 3D model is to open up new possibilities for device characterisation both quantitatively and qualitatively. Although techniques have been presented to prevent trapped mode resonances [40] and reduce leakage through substrate resonances [41], the full 3D model can be a useful verification at the last step of the design process. There is much room for improvement in the nonlinear part of the device modeling, further discussed in Sec. 6. The full 3D model is the only presented technique so far to account for instabilities, diode yield or specific diode failures. More of this will be presented in Sec. 4.3.

As intended, we can use the full 3D model to validate the assumptions of the unit cell model. Fig. 4.3. shows the fundamental frequency power received by diodes in different columns in the full 3D model together with the 1st unit cell assumption. The phase of the fundamental frequency voltages are also plotted. There is a maximum normalized amplitude deviation of 0.15 and a maximum phase deviation of 1 degree between the two models. We can conclude that the result provided by the full 3D model only slightly deviates from the assumed one and the assumption remains valid.

The 2nd assumption states that the multiplier array solely excites the fundamental waveguide mode at the output frequency. To get a quantitative overview of this, we plot the third harmonic voltages, currents and powers in Fig. 4.4. both from the full 3D and unit cell model. The unit cell amplitudes show good agreement with the sinusoidal curve. The full 3D model however, presents abrupt changes in

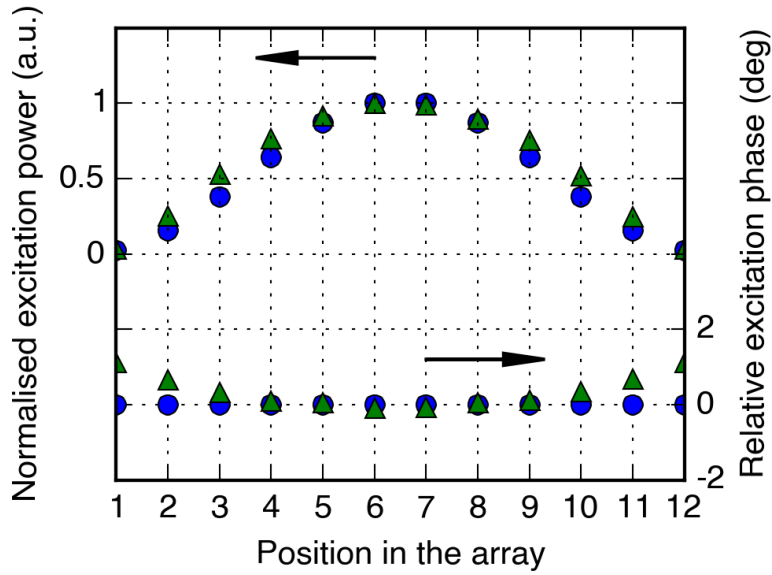


Figure 4.3: Input power and phase distribution among different columns of the array: unit cell assumption (circles) and full 3D model (triangles).

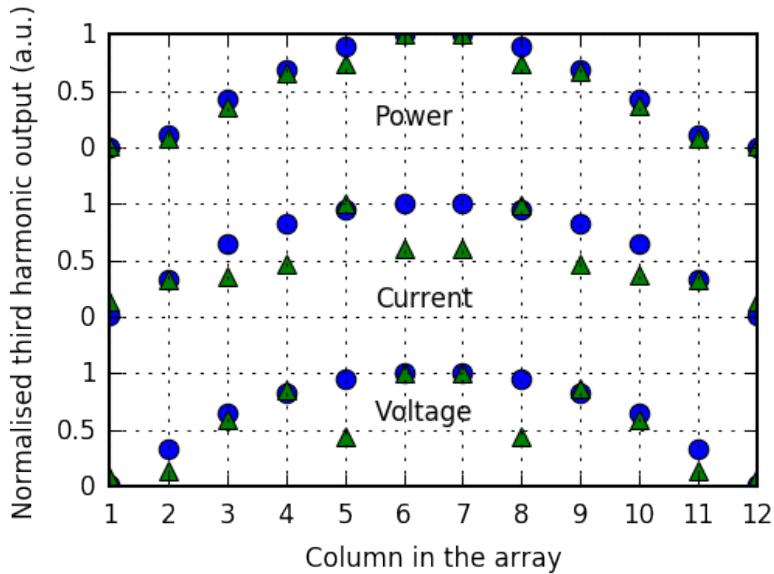


Figure 4.4: Magnitude distribution of the third harmonic power, current and voltage of the diodes in different columns for 300 mW input power at 247 GHz output frequency in the full 3D model (triangles) and in the unit cell model (circles).

both currents and voltages at some particular columns. As a result of this the power distribution will deviate from a \sin^2 and therefore higher order modes will be excited. The reason for the abrupt amplitude changes can be understood by observing the multiplier array and filter. The cross sectional view of them (hiding the InP substrate) is shown in Fig. 4.7. As can be seen, distinct columns of the multiplier array overlap with the metallization of the filter while others overlap with the apertures.

Since, for design purposes, the distance between the multiplier array and the filter is $0.5\lambda_g$ at the input frequency, the filter is not observed as a homogeneous surface and the half guided wavelength introduces short circuit for the diode overlapped with the metal parts.

The excitation of higher order modes is a benchmark problem in every device implemented in a guided wave environment. In [16] it was presented that a mode decomposition can be carried out based on the spatial Fourier transformation of the diode output powers. However, this technique only accounts for the higher order mode excitation resulting from the diode nonlinearity. This example shows how the linear electromagnetic can introduce higher order mode excitation and how this is beyond the limits of the unit cell modeling technique.

I-V Dynamic Load Line (DLL) plots are a common way to investigate one pump cycle of a diode in a frequency multiplier. DLL plots of all the diodes are plotted in Fig. 4.5. with the same scale at their corresponding position in the array. The breakdown voltage of the diodes is estimated to be 33 V [17], and one can obtain from the data of Fig. 4.5. that diodes in the middle column are only pumped with 9.2 V. This corresponds to the medium input power mentioned in Sec. 4.1.

Fig. 4.6. shows the quasi-impedances and embedding impedances of the diodes in different columns at the fundamental- and output frequency, respectively, defined as:

$$Z_{quasi f_p} = \frac{V_{f_p}}{I_{f_p}} \quad (4.1)$$

$$Z_{embedding f_{3p}} = -Z_{quasi f_{3p}}. \quad (4.2)$$

The quasi-impedance at the fundamental frequency is very similar across the array. The small difference is most likely originating from the uneven excitation of the diodes. The embedding impedances at the output frequency however, show great differences between diodes. It is worth noting that the diode with the metallization in the back experience a capacitive embedding impedance. The side column also differs greatly from column number 3,4,6, which can be explained with the low input power and thus low conversion efficiency at the side columns.

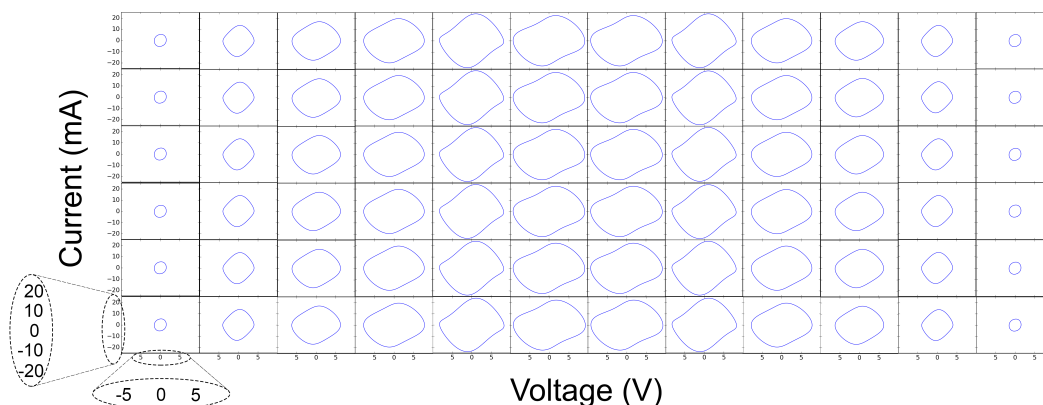


Figure 4.5: I-V Dynamic Load Line plot for every diode in the array at 247 GHz output frequency and 300 mW input power.

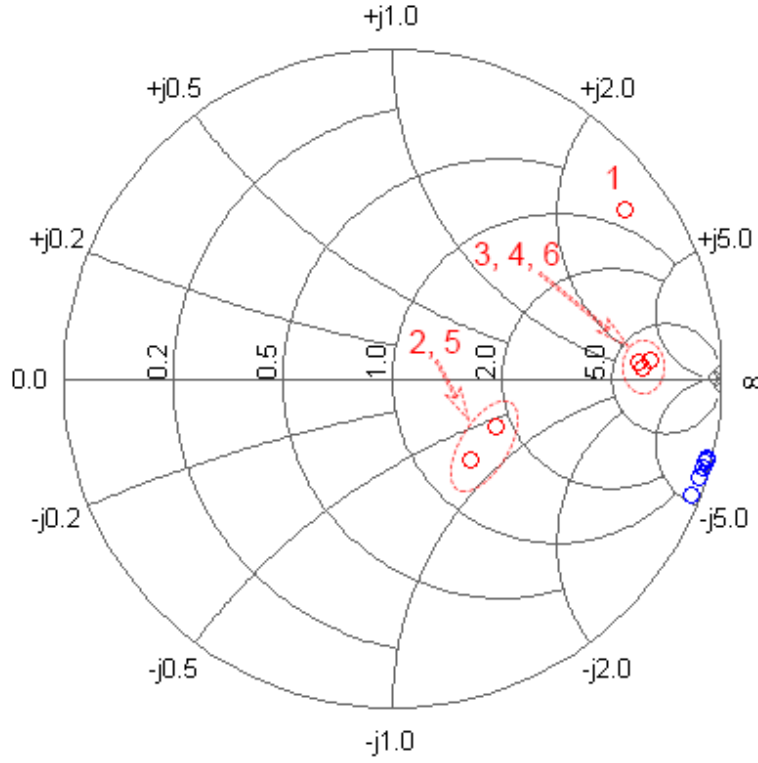


Figure 4.6: Quasi-impedances (blue) and embedding impedances (red) of diodes in different columns at the fundamental- and output frequency of 82.333 GHz and 247 GHz, respectively. Number of the column the diode is located in is indicated for the embedding impedances. The Smith-Chart is normalized to 50 Ω .

The 3rd assumption of the unit cell method describes how the contributions from the diode third harmonic powers are combined at the output. The unit cell model uses ideal power combiners, meaning that $S_{iM} = S_{jM}$, where i and j are diode ports and M is the output port. On the other hand, examining the S-parameters obtained from the full 3D model, it is clear that the contributions not only have a phase difference, but different amplitudes as well. This example shows the contributions from different columns of the array ($i=1\dots 6$) to the output waveguide port (M) at 247 GHz.

$$S_{iM} = \begin{bmatrix} 0.0055 \angle -63.3^\circ \\ 0.035 \angle -59.8^\circ \\ 0.046 \angle -62.7^\circ \\ 0.054 \angle -62.9^\circ \\ 0.087 \angle -60.5^\circ \\ 0.071 \angle -63.1^\circ \end{bmatrix} \quad (4.3)$$

This confutes the assumption about ideal power combining. Moreover, these S-parameters can only be obtained using the full 3D model.

The 4th assumption of the unit cell method is, by definition, violated but hard to quantitize. The infinite array assumption of the unit cell model assumes a free-space

	Unit cell model		Full 3D model	
	f_p	$3f_p$	f_p	$3f_p$
No. Tetrahedrons	$7.4 \cdot 10^3$	$2.0 \cdot 10^4$	$3.6 \cdot 10^5$	$1.2 \cdot 10^6$
Time	2 min	14 min	50 min	4 h

Table 4.1: Number of tetrahedrons and time required to obtain the FEM solution for each model per frequency point.

impedance (377Ω) as port impedance. However, the characteristic impedance in a rectangular waveguide is a function of frequency, and only approaches the free-space impedance as the wavelength decreases and the waveguide gets overmoded (Z_C at f_p in our example is around 540Ω , while at $3f_p$ it approaches 377Ω). This results in a mismatch in impedances and is a possible contribution to the frequency shift in the unit cell model's result.

To examine the 5th assumption we compared columns that are supposed to have equal currents and voltages. Among the fundamental frequency voltages and current, there was an error less than 1%, whereas among the third harmonic currents and voltages the highest error was 5.7%. This is most likely due to the convergence criteria of the HB simulation.

Table 4.1 summarizes the computational needs of two models in terms of time and number of tetrahedrons required to obtain a FEM solution. The time requirement is obtained from solutions on a computer utilising 2 processors of 2.4 GHz with 8 cores each, after optimizing the initial mesh setup. It can be seen that the unit cell model is computationally extremely cheap, and yet the full 3D model is also very accessible despite its size and complexity.

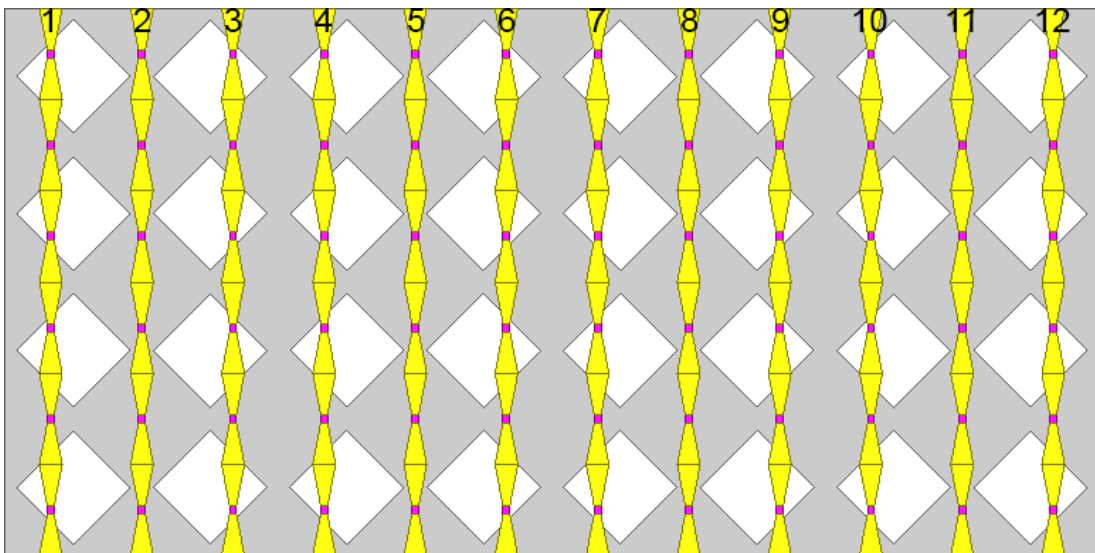


Figure 4.7: Cross sectional view of the antenna array, perpendicular to the direction of propagation. The InP substrate is hidden therefore the output filter is visible in the background and the columns of the multiplier array are numbered.

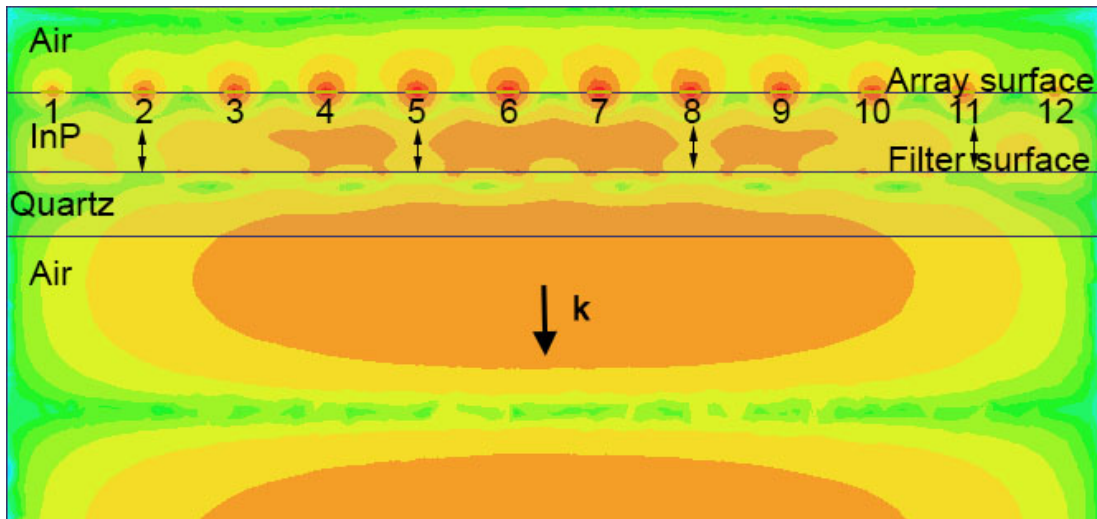


Figure 4.8: Electric field distribution of the multiplier array from a top cross sectional view. The direction of propagation, the column numbers and the material of the different media are indicated. Arrows mark the standing waves short circuiting the particular diode columns.

4.3 Failure analysis

Quasi-optical array devices have the advantage over their conventional counterparts of being resistant to device failures to a certain extent. As the full 3D model includes the coupling between individual antennas in the array, it is very tempting to investigate the consequences of diode failures. In this section we examine two possible failure cases:

Mechanical fracture of the airbridge can happen at any position of the array, therefore both the number of broken airbridges and the position of the fracture are interesting to investigate.

Fig. 4.10. shows a map of the output power versus single diode failure over the array. As expected, the diodes in the middle columns has the most serious impact on device performance and degrade the output power the most in case of failure. Notice that a single failure at the edge columns surprisingly introduces a gain in output power. A possible explanation for this is that the total input power is not high enough for them to work in saturated efficiency mode and therefore presenting a large reactance for their neighboring diode may result in a higher overall efficiency than the small efficiency contributions that they initially provide. Simulating with two failed diodes (one on the sides) shows degradation in the output power.

We also carried out a large number of simulations for open circuit diode failures from $n=1$ to $n=71$ diodes to gain a statistical distribution. For each simulation, the position of the fracture(s) were assigned randomly. The simulation was controlled through a VBA script. The averaged output power versus diode failure follows an exponentially decaying curve and is shown in Fig. 4.11. Results show a 3 dB decrease of output power for the failure of 14% of the total diodes.

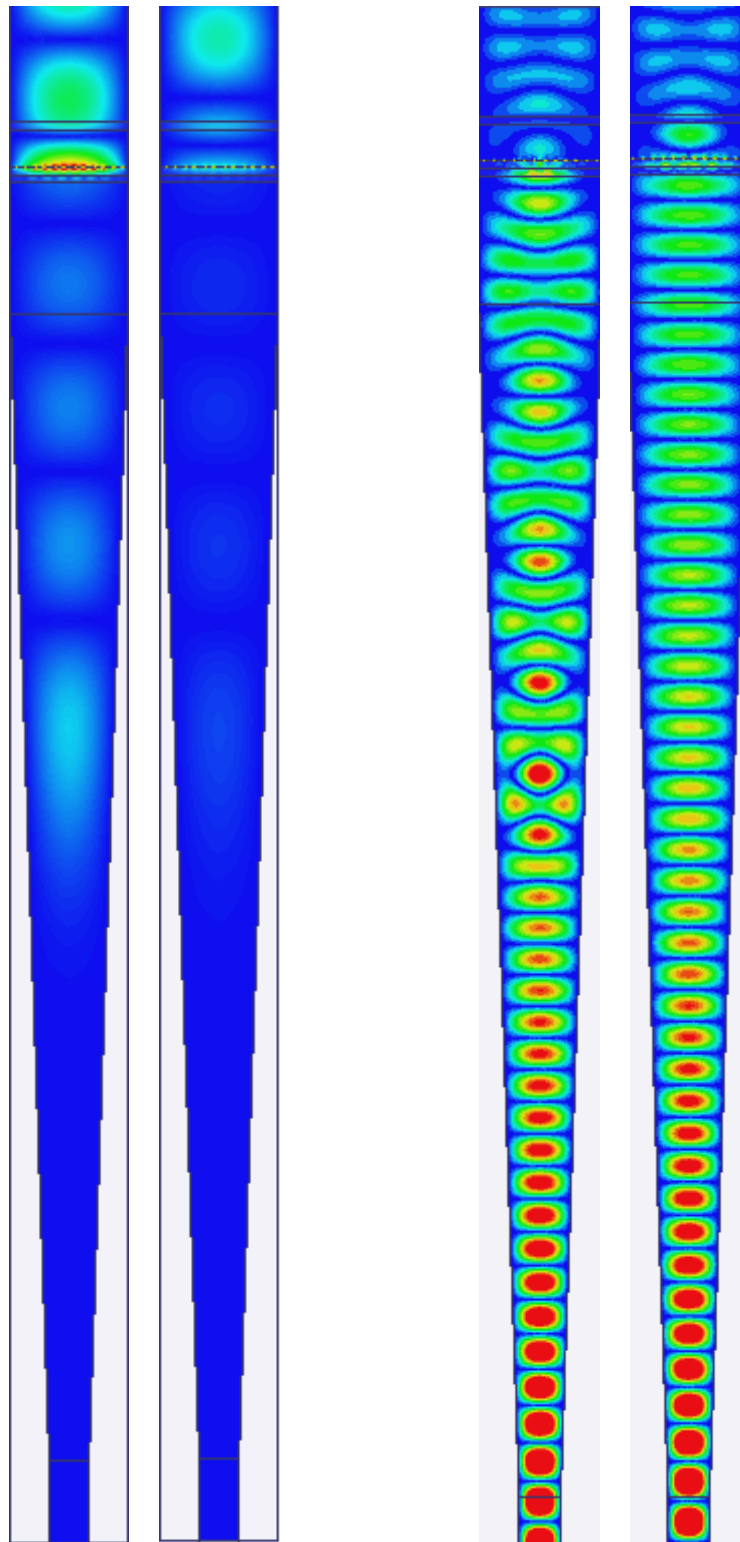


Figure 4.9: Electric field along the device for the fundamental frequency and the third harmonic. 2 plots with 90 degrees phase shift between them are assigned for both frequencies in order to show the standing waves between the taper and the multiplier array.

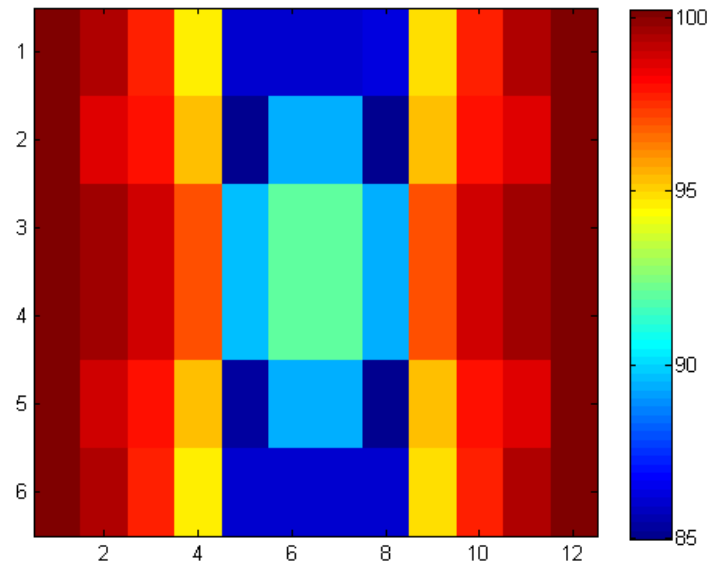


Figure 4.10: Percentage of output power versus failure of a single diode mapped over the multiplier array.

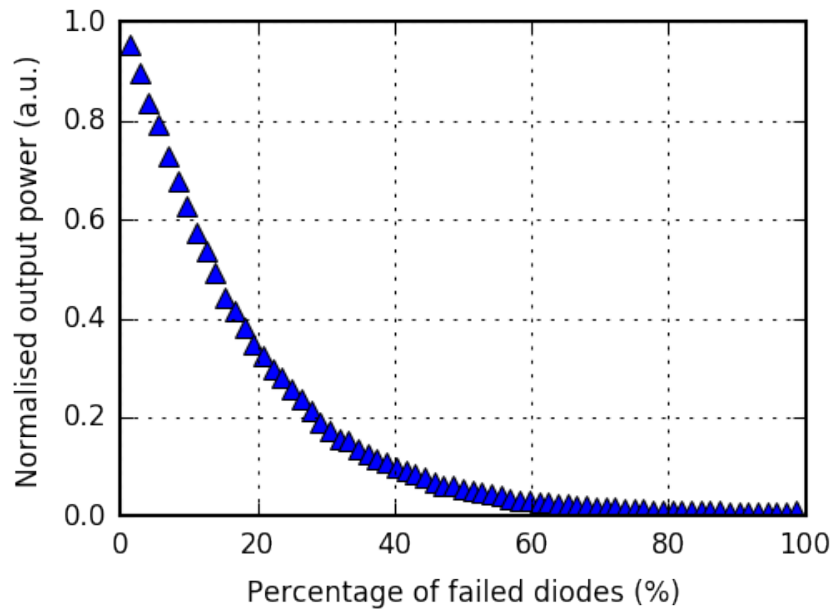


Figure 4.11: Percentage of output power versus number of open circuit diode failures.

5

New filter design and implementation

5.1 Design

The results described in Section 4.2 motivate the design of a new filter. The idea is to prove that just by changing the periodicity of the output filter, an excitation much closer to a single mode can be achieved at the multiplier array and the total output power can be increased. For this, we design an output filter which has the similar periodicity as the multiplier array (6x12) and the same S-parameters as the original output filter.

An in-depth discussion about the design of frequency selective surfaces can be found at [42]. Generally, for a unit cell geometry of a conductive patch having an arbitrary shape there is always a wavelength which has a current maxima and therefore the whole structure has a transmission zero. In case of non-loaded patches this wavelength is more or less the circumference of the geometry. For every kind of grid there exists a so-called complementary grid, which is an aperture of the same geometry on a golden surface. The relation for the transmission and reflection coefficients of the original and complementary grid is $r = t_c$ and $t = r_c$. To decrease the unit cell size of a FSS one has to present capacitance which is inversely proportional to the resonance frequency.

$$f_0 \sim \frac{1}{\sqrt{LC}} \quad (5.1)$$

The cross-shaped aperture grids has got considerable attention and their behaviour is described with empirical equations in [43]. It has a higher capacitance than the rhomb shape and thus able to compensate for the reduced size. This suits well with our design purposes. The exact geometry was obtained through optimization in HFSS and shown in Fig. 5.1.

5.2 Simulation results

5.2.1 S-parameter characterisation

The two filters were characterised through simulations and measurements. A simulation with periodic boundary conditions was carried out on both of the unit cells as well as a simulation with waveguide boundary conditions on both of the filters.

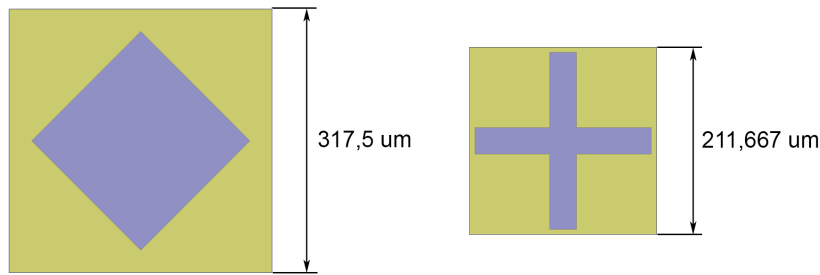


Figure 5.1: Unit cell geometry and size of the two filters.

185 μm InP was included in the input port and Quartz was present at the output, which got deembedded until the filter surface for every simulation.

The simulated scattering parameters using waveguide boundary conditions are shown in Fig. 5.2. The two filters have a 0.5 dB maximum insertion loss difference and a 0.02 dB maximum return loss difference over the frequency bands of interest. We conclude that they show a negligible difference in terms of S-parameters.

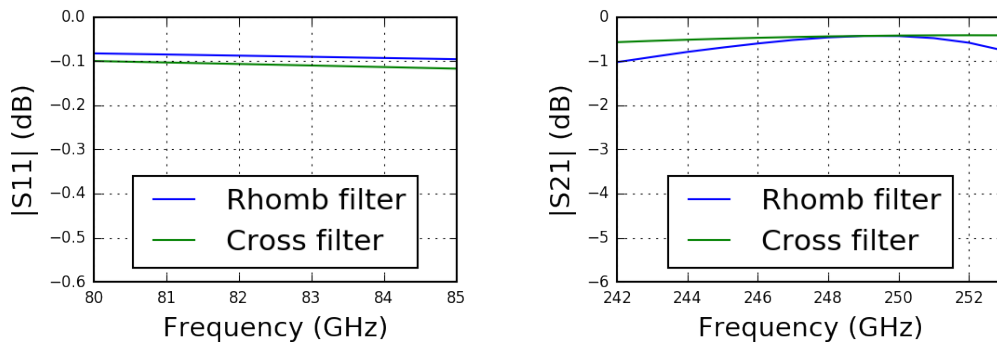


Figure 5.2: Simulated S-parameters showing the similarities between the two filters.

5.2.2 RF characterisation

The multiplier was modeled using the full 3D model presented in Sec. 3.4. The exact same linear model was solved twice with both filter pattern in Ansys HFSS, then solved using Harmonic Balance technique in NI Microwave Office with the same non-linear elements. Fig. 5.3. shows the third harmonic output power of the multiplier for both filters versus output frequency for 300 mW input power, and Fig. 5.4. shows the third harmonic output power for both filters versus first harmonic input power at 247 GHz output frequency. The multiplier using the cross filter presents 1 dB higher peak output power than the one using rhomb filter.

Fig. 5.5. shows the third harmonic currents, voltages, and powers of the diode for both devices. It can be seen that the device with the cross filter is closer to a single moded excitation than the device with the rhomb filter.

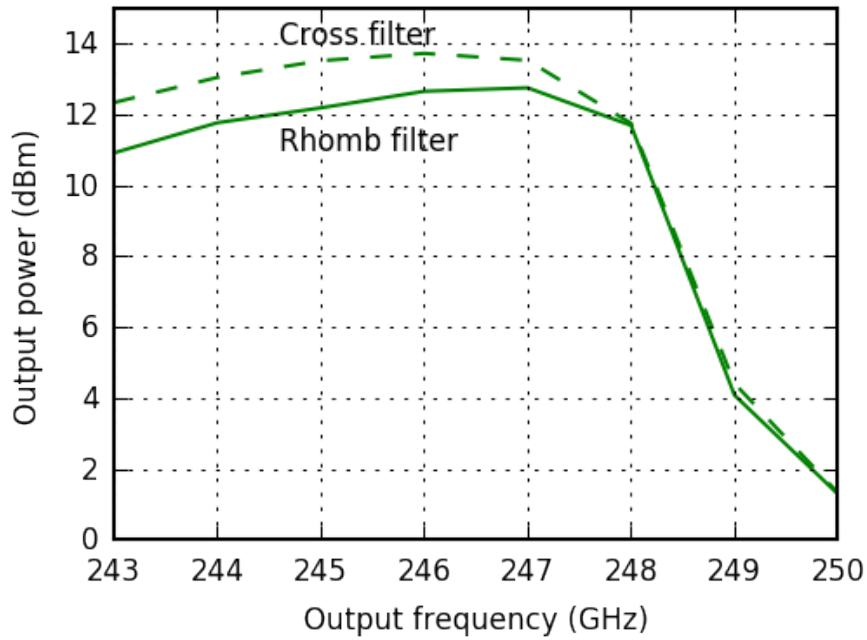


Figure 5.3: Simulated frequency sweep of the devices with two different filters.

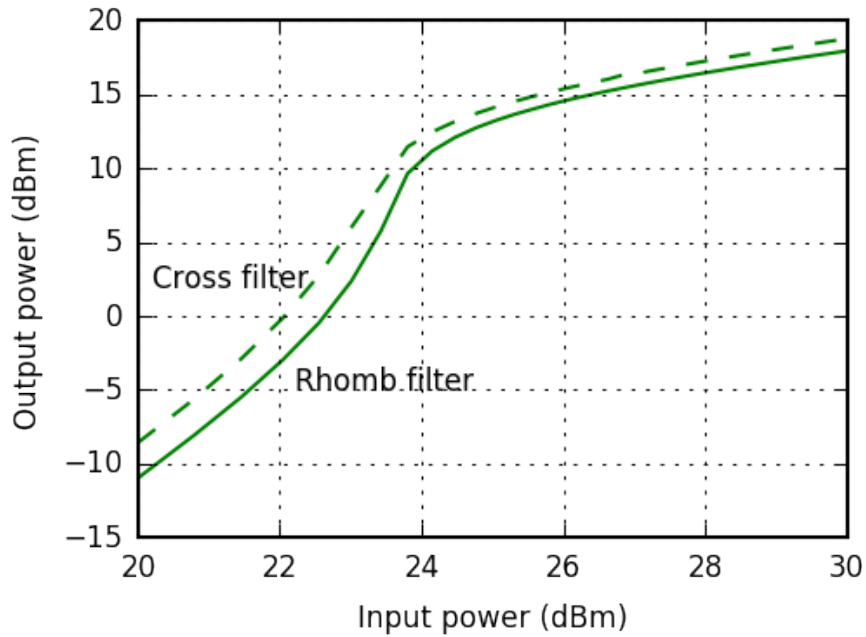


Figure 5.4: Simulated power sweep of the devices with two different filters.

To quantize this, we performed Discrete Fourier-transform (DFT) on the diode third harmonic powers defined as

$$P_{f_3} = \frac{1}{2} V_{f_3} I_{f_3}^* \quad (5.2)$$

We only took into account the variation among diodes in the same row of the

	TE ₁₀	TE ₃₀	TE ₅₀	TE ₇₀	TE ₉₀
Rhomb filter	1.0	0.032	0.016	0.054	0.026
Cross filter	1.0	0.004	0.001	0.003	0.017

Table 5.1: DFT coefficients for the excited TE_{n0} modes for the two filters (normalized to TE₁₀).

grid. This assumption restricts us to distinct between TE_{n0} modes only, but this is enough to prove the importance of filter periodicities. The obtained DFT coefficients are shown in Table 5.1. Fig. 5.6. shows the electric field distribution from a top cross sectional view in the device with new filter at the output frequency. It can be observed that the standing waves appearing on Fig. 4.8 are absent and the power contributions from different diodes combine to a propagating field close to TE₁₀. To further demonstrate, Fig. 5.7. shows the electric field distribution along both of the devices from a top cross sectional view. There are two plots dedicated for each device with a phase shift of 90 degree between them. This is in order to show how higher order modes create standing waves between the taper and the array in the device with rhomb filter. This is absent in the device with cross filter.

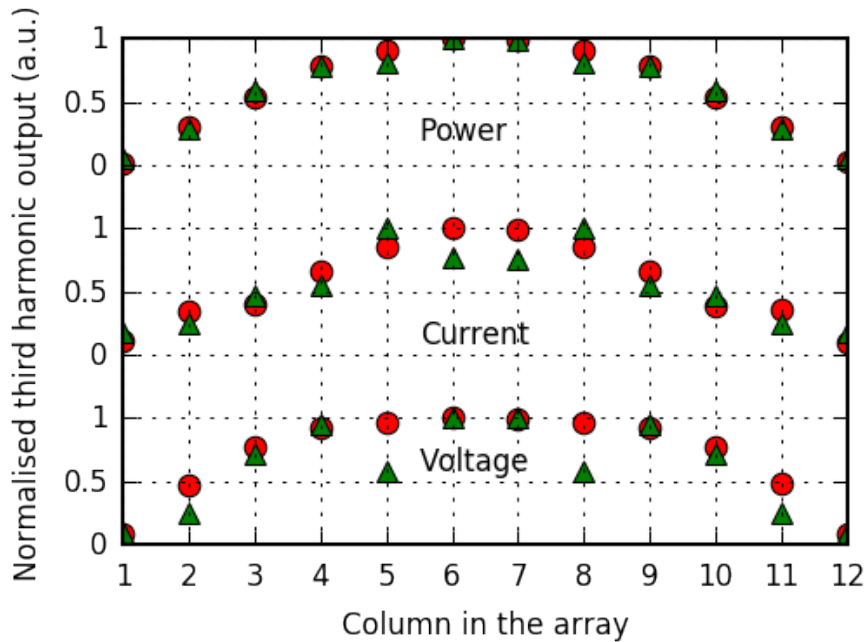


Figure 5.5: Magnitude distribution of the third harmonic power, current and voltage of the diodes in different columns for 300 mW input power at 247 GHz output frequency for the device with rhomb filter (triangles) and the device with cross filter (circles).

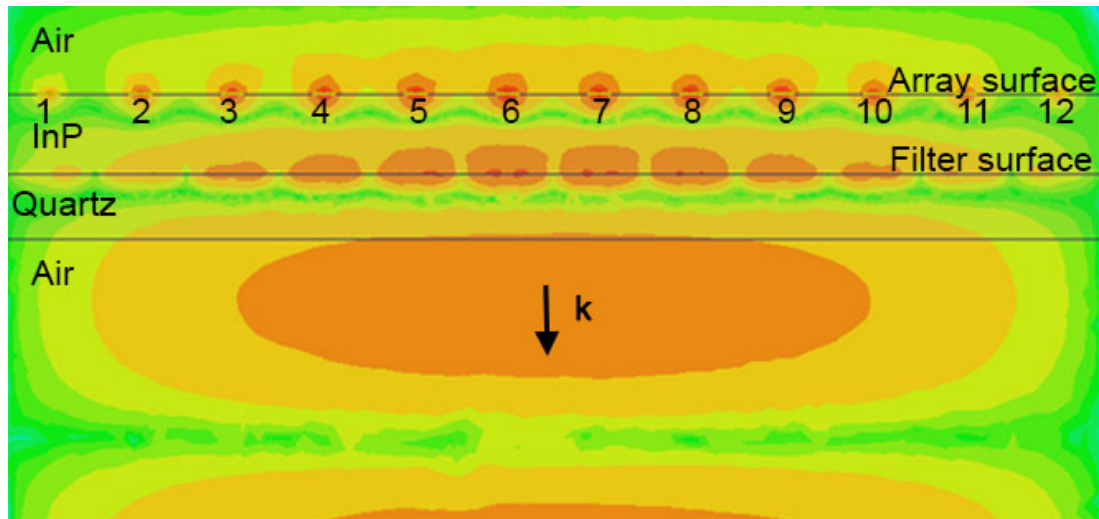


Figure 5.6: Electric field distribution of the multiplier array with the cross filter from a top cross sectional view. The direction of propagation, the column numbers and the material of the different media are indicated.

5.3 Fabrication

The filter was fabricated using electron beam lithography on 250 μm Quartz substrate which was then polished from the back side to 150 μm . Two layers of resist has been evaporated and the pattern was exposed by electron beam. Processing on Quartz substrate induce two main challenges: the transparency of the material in the optical region makes it hard to judge the pattern development, and the bad conducting of the material allows charges to be built up on the wafer and distort the drawn pattern. 100 Angstrom Titanium was deposited to provide a better bonding to the surface, then 1 μm Gold was deposited. The deposition was performed in a vacuum of $1\text{e-}6$. The lift-off was made in acetone and the lower layer resist was removed, thus leaving the gold pattern on the substrate.

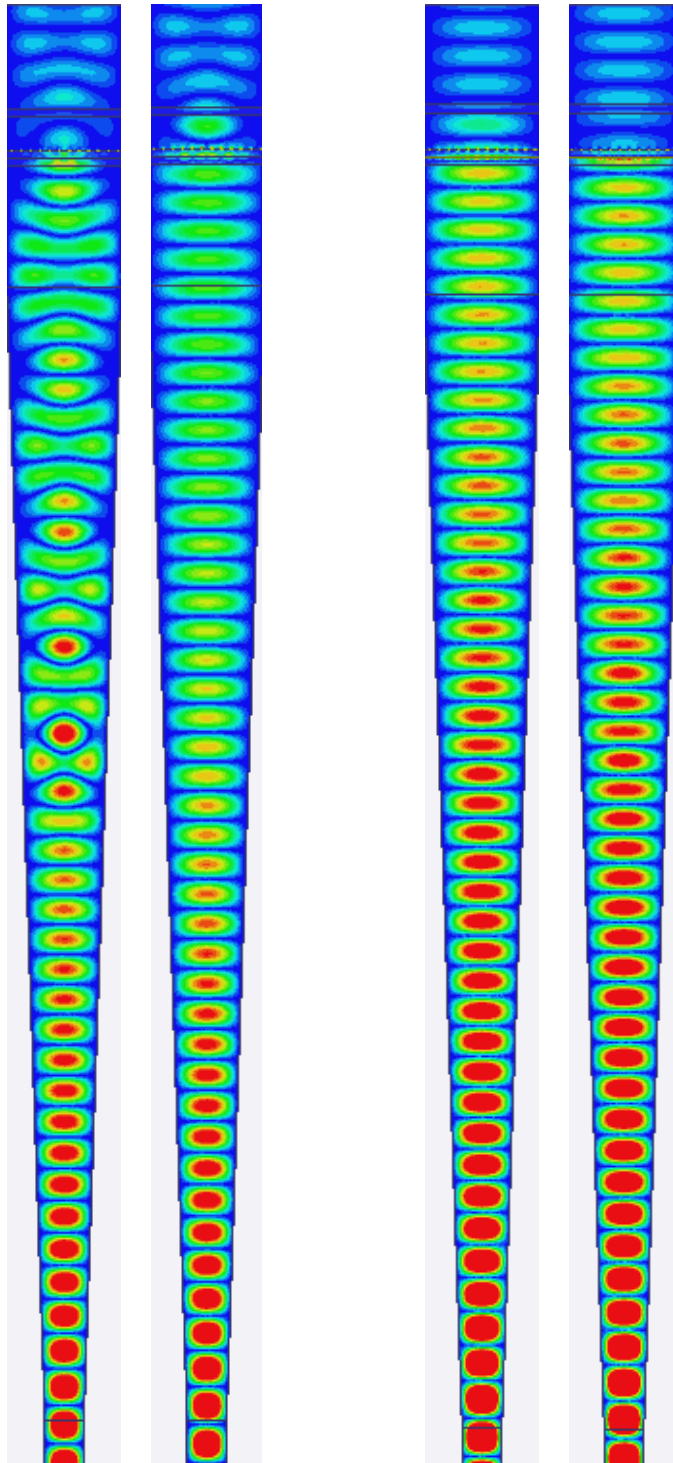


Figure 5.7: Cross-sectional plots of the electric field in the devices. Both devices are plotted twice with a 90 degree phase shift between the plots in order to show the mode distribution.

5.4 Measurements

5.4.1 VNA measurements

In order to show that the two filters are identical from a macro electromagnetic point of view, S-parameter measurements were carried out. The relevant parameters to measure are the reflection at the fundamental frequency and the transmission at the output frequency. Only the filters on the Quartz substrate were assembled in a waveguide shim, excluding the InP in order to reduce the error coming from assembly uncertainties. This way the results do not represent any role in the circuit's principle of operation, but enough to show the similarity between the filters. The reflection at the input frequency band is easily measured with the corresponding frequency extenders as the calibration at this frequency is not challenging. Fig. 5.8. shows the similarity between the two filters, the maximum amplitude difference between their S11 parameter is 0.02.

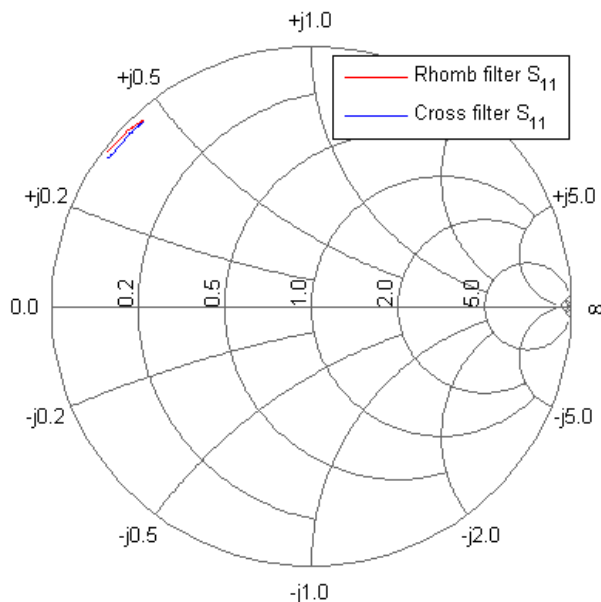


Figure 5.8: Reflection coefficient of the filters at the input frequency band (80-85 GHz).

Measuring the transmission at the third harmonic is challenging as the filters are mounted in a WR10 waveguide which is overmoded at that band and the frequency extender designed for the output frequency band has a WR3 size flange. However, using two WR10-WR3 linear tapers we can bridge the waveguide size differences. The measurement setup is shown in Fig. 5.9. The reference planes to which the measurement was calibrated are depicted with dashed lines. To exclude the losses caused by the tapers we can exclude the DUT and carry out a measurement on the two tapers. The parameter of interest is then simply

$$S_{21}^{DUT} = S_{21}/S'_{21} \quad (5.3)$$

where S_{21} is the S-parameter measured in the setup shown in Fig. 5.9., S'_{21} is the S-parameter measured without the DUT, and the S_{21}^{DUT} is the S-parameter of the DUT. The measurement result has dips as high as 10 dB and therefore considered too noisy to draw any conclusion from. This is most likely due to the many discontinuities that the measurement setup contained.

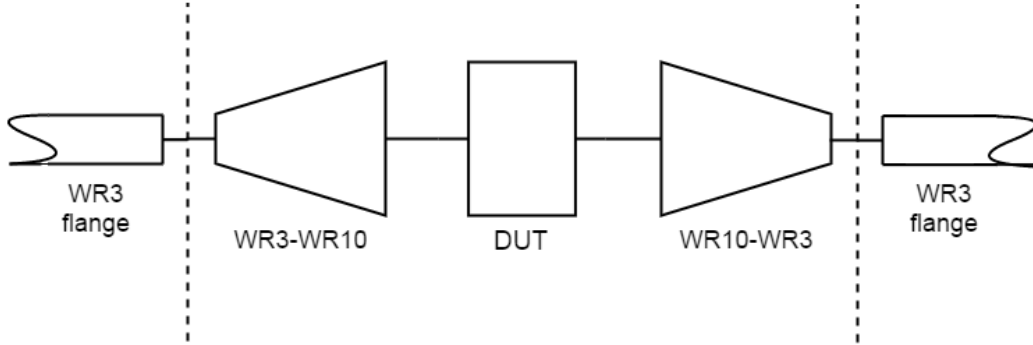


Figure 5.9: Schematic of the setup to measure the S-parameters of the two filters at the output frequency band.

5.4.2 RF measurements

RF measurements were carried out with the multiplier array assembled with both filters individually. The measurement setup is identical to the one described in Sec. 3.1. with the exception of the input matching network. The input matching network in this measurement is a tunable waveguide slab presented in [17]. Thanks to the smart mechanical design, the InP matching slab can be moved in order to match the input side of the multiplier at each frequency point.

The results are plotted in Fig. 5.10. The new filter managed to exceed the output power of its predecessor only at the lower part of the frequency band. The device is very sensitive to small dimension changes and thus we carried out multiple measurements after hand-lapping the filter substrate down by approximately 10 *um* each step. These results are also visible in Fig. 5.10., showing that a 10 *um* substrate thickness difference can lead to an output power difference of 5 dB.

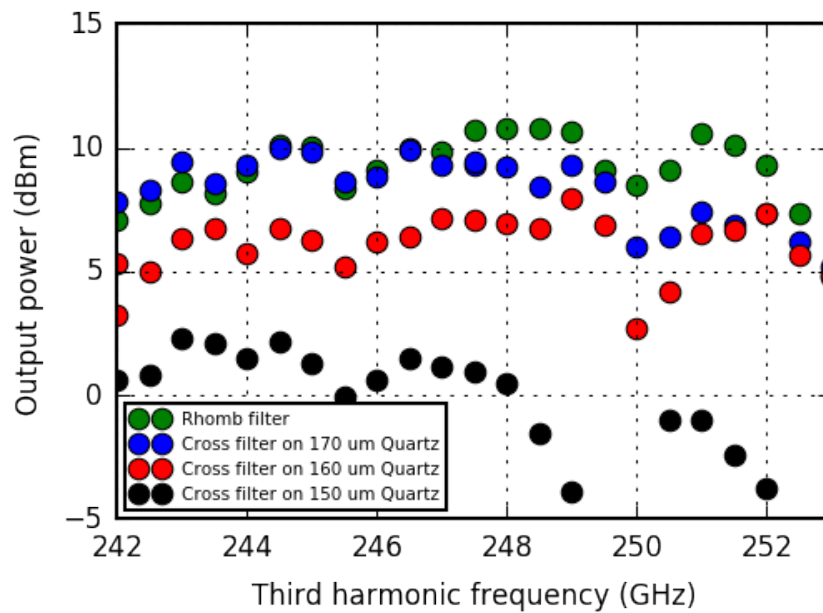


Figure 5.10: Measured output power of the multiplier array with different output filters for 300 mW input power. The input matching slab was tuned for maximum conversion efficiency at each frequency point.

6

Conclusions and future work

A full 3D electromagnetic model have been presented for waveguide-embedded frequency multiplier arrays. The model was verified by measurements on a frequency multiplier array operating at 250 GHz output frequency and was compared to a traditionally used unit cell model. The unit cell model is a computationally cheap approach, which is a proper choice for the first stage of the design procedure. The full 3D model includes the interaction between all the nonlinear elements and thus more reliably predicts the output power curve versus frequency and input power. Furthermore, by solving the exact geometry in a 3D electromagnetic solver and presenting every nonlinear elements in a Harmonic Balance simulation, the full 3D model broadens the possibilities in device characterisation. Thus it can be used to reveal and prevent undesired mechanisms in the design before fabrication.

The full 3D model can also be further improved as a future work in many ways. The output power of the multipliers start to saturate for increasing input powers as the device temperature starts to play an important role. To implement a self-consistent electro-thermal model is an extensive work. First an electro-thermal HBV model has to implemented into the circuit simulator [26]. Afterwards a 3D thermal simulation of the device would have to be carried out, the mesas as heat sources and the waveguide walls as boundary conditions. The result is a thermal resistance matrix which takes into account not only the self-heating but the mutual thermal coupling. This thermal matrix then would be coupled to the electro-thermal HBV model in the circuit simulator [44], resulting in a self-consistent electro-thermal model which provides temperature feedback to the nonlinear models according to their, and their neighbours' dissipated power. Accounting for the diode yield can also be implemented in the full 3D model. By measuring the CV curve of each diode, one can tailor the nonlinear model used across the array accordingly. The large number of nonlinear elements raises stability issues as well. Although not observed during this work, different solutions could be obtained depending on the previous state of the nonlinear currents and voltages. Experimentally verifying such case would ultimately validate the full 3D model.

The full 3D model can also be used for advanced device design. The biggest challenge of frequency multiplier array design is to even out the conversion efficiency over the grid of elements. It is only possible to present the same embedding impedance to the diodes along the array in this configuration, and different power levels result in varying efficiency. However, with the full 3D model the diodes could be tailored (with e.g. tapered mesa area) to perform similar efficiency for the same embedding impedances. [45] Another advanced design concept is to illuminate the array with an overmoded waveguide configuration in order to even out the excitation

power along the diodes. A combination of TE_{n0} (where n is an odd number) modes seems promising as they maintain the TE_{10} electric symmetry and field distribution is vertically invariant.

There is still room left to develop advanced measurement setups in order to gain further knowledge and proof about the operation of such devices. Measurements with a spectrum analyzer could reveal low frequency intermodulation products originating from resonances in the structure. The taper connected to the output of the device could also be replaced with a horn antenna, then perform a planar scan with a second test antenna. With extensive work, the mode distribution of the excited field in the frequency multiplier array could be extracted.

Overall, the suggested design methodology for waveguide-embedded frequency multiplier arrays is to first iterate using the unit cell method, then later fine tune and improve the design using the full 3D model. As the computational resource availability continues to grow rapidly, the full 3D model is becoming a more and more accessible tool.

Bibliography

- [1] P. Siegel, "Terahertz Technology," *IEEE Trans. Microw. Theory Techn.*, vol. 50, no. 3, pp. 910–928, Mar. 2002.
- [2] T. G. Phillips and J. Keene, "Submillimeter astronomy," *Proceedings of the IEEE*, vol. 80, no. 11, pp. 1662–1678, Nov 1992.
- [3] E. Pickwell and V. P. Wallace, "Biomedical applications of terahertz technology," *Journal of Physics D: Applied Physics*, vol. 39, no. 17, pp. R301–R310, Aug. 2006.
- [4] P. F. Taday, "Applications of terahertz spectroscopy to pharmaceutical sciences," *Philosophical Transactions of the Royal Society A: Mathematical, Physical and Engineering Sciences*, vol. 362, no. 1815, pp. 351–364, Feb. 2004.
- [5] K. Cooper, R. Dengler, N. Llombart, T. Bryllert, G. Chattopadhyay, E. Schlecht, J. Gill, C. Lee, A. Skalare, and I. Mehdi, "Penetrating 3-D Imaging at 4-and 25-m Range Using a Submillimeter-Wave Radar," *IEEE Trans. Microw. Theory Techn.*, vol. 56, no. 12, Part 1, pp. 2771–2778, 2008.
- [6] T. Bryllert, K. B. Cooper, R. J. Dengler, N. Llombart, G. Chattopadhyay, E. Schlecht, J. Gill, C. Lee, A. Skalare, I. Mehdi, and P. H. Siegel, "A 600 GHz imaging radar for concealed objects detection," in *2009 IEEE Radar Conference*. IEEE, pp. 1–3.
- [7] C. H. Page, "Frequency conversion with positive nonlinear resistors," *J Res Nat Bur Stand*, vol. 56, no. 4, April 1956.
- [8] R. H. Pantell, "General power relationships for positive and negative nonlinear resistive elements," *Proceedings of the IRE*, vol. 46, no. 12, pp. 1910–1913, Dec 1958.
- [9] G. Chattopadhyay, "Technology, Capabilities, and Performance of Low Power Terahertz Sources," *IEEE Trans. THz Sci. Technol.*, vol. 1, no. 1, pp. 33–53, 2011.
- [10] J. W. Mink, "Quasi-Optical Power Combining of Solid-State Millimeter-Wave Sources," *IEEE Trans. Microw. Theory Techn.*, vol. 34, no. 2, pp. 273–279, Feb. 1986.
- [11] A. Mortazawi, T. Itoh, and J. Harvey, *Active antennas and quasi-optical arrays*. IEEE Press, 1998.
- [12] M. Kim, E. A. Sovero, J. B. Hacker, M. P. DeLisio, J.-C. Chiao, S.-J. Li, D. R. Gagnon, J. J. Rosenberg, and D. B. Rutledge, "A 100-Element HBT Grid Amplifier," *IEEE Trans. Microw. Theory Techn.*, vol. 41, no. 10, pp. 1762–1771, 1993.

- [13] J. A. Higgins, E. A. Sovero, and W. J. Ho, "44-GHz monolithic plane-wave amplifiers," *IEEE Microwave and Guided Wave Letters*, vol. 5, no. 10, pp. 347–348, Oct 1995.
- [14] J. Birkeland and T. Itoh, "A 16 Element Quasi-Optical FET Oscillator Power Combining Array with External Injection Locking," *IEEE Trans. Microw. Theory Techn.*, vol. 40, no. 3, pp. 475–481, 1992.
- [15] J. Bae, M. Fujita, and K. Mizuno, "A W-band overmoded-waveguide oscillator with Gunn diodes," *IEEE Trans. Microw. Theory Techn.*, vol. 49, no. 12, pp. 2554–2559, Dec 2001.
- [16] S. A. Rosenau, "Quasi-optical overmoded waveguide frequency multiplier grid arrays," Ph.D. dissertation, University of California Davis, 2001.
- [17] R. Dahlbäck, J. Vukusic, R. M. Weikle, II, and J. Stake, "A Tunable 240 — 290 GHz Waveguide Enclosed 2-D Grid HBV Frequency Tripler," *IEEE Trans. THz Sci. Technol.*, vol. 6, no. 3, pp. 503–509, May 2016.
- [18] A. Moussessian, M. Wanke, Y. Li, J.-C. Chiao, J. Allen, T. Crowe, and D. Rutledge, "A terahertz grid frequency doubler," *IEEE Trans. Microw. Theory Techn.*, vol. 46, no. 11, pp. 1976–1981, 1998.
- [19] J. Schellenberg, E. Watkins, M. Micovic, B. Kim, and K. Han, "W-band, 5W solid-state power amplifier/combiner," *IEEE MTT-S Int. Microw. Symp. Dig.*, pp. 240–243, 2010.
- [20] B. Schumann, M. Hoft, M. Saglam, H. Hartnagel, and R. Judaschke, "A 5 element 450 GHz HBV frequency tripler," *IEEE MTT-S Int. Microw. Symp. Dig.*, vol. 2, pp. 759–762, 2003.
- [21] W. W. Lam, H. Chen, D. B. Rutledge, C. F. Jou, and N. C. Luhmann Jr, "Diode-grids for millimeter-wave phase-shifters and frequency doublers," in *Antennas and Propagation Society, International Symposium*, 1987, pp. 1190–3.
- [22] J. B. Hacker, A. L. Sailer, B. Brar, G. Nagy, R. L. J. Pierson, and J. A. Higgins, "A high-power W-band quasi-optical frequency tripler," *IEEE MTT-S Int. Microw. Symp. Dig.*, vol. 3, pp. 1859–1862, 2003.
- [23] E. L. Kollberg and A. Rydberg, "Quantum-barrier-varactor diodes for high-efficiency millimetre-wave multipliers," *Electronics Letters*, vol. 25, no. 25, pp. 1696–1698, 1989.
- [24] M. Ingvarson, B. Alderman, A. O. Olsen, J. Vukusic, and J. Stake, "Thermal Constraints for Heterostructure Barrier Varactors," *IEEE Electron Device Lett.*, vol. 25, no. 11, pp. 713–715, Nov. 2004.
- [25] L. Dillner, J. Stake, and E. L. Kollberg, "Modeling of the heterostructure barrier varactor diode," *Int. Semicond. Device Research Symp*, pp. 179–182, 1997.
- [26] M. Ingvarson, J. Vukusic, A. Olsen, T. A. Emadi, and J. Stake, "An electro-thermal HBV model," *IEEE MTT-S Int. Microw. Symp. Dig.*, pp. 1151–1153, 2005.
- [27] P. Penfield and R. P. Rafuse, *Varactor Applications*. MIT Press, 1962.
- [28] E. L. Kollberg, J. Stake, and L. Dillner, "Heterostructure barrier varactors at submillimetre waves," *Philosophical Transactions: Mathematical, Physical and Engineering Sciences*, vol. 354, no. 1717, pp. 2383–2398, 1996.

-
- [29] J. Stake, S. H. Jones, L. Dillner, S. Hollung, and E. L. Kollberg, "Heterostructure-barrier-varactor design," *IEEE Trans. Microw. Theory Techn.*, vol. 48, no. 4, pp. 677–682, 2000.
- [30] L. Dillner, J. Stake, and E. L. Kollberg, "Analysis of symmetric varactor frequency multipliers," *Microwave Opt. Technol. Lett.*, vol. 15, no. 1, pp. 26–29, May 1997.
- [31] D. B. Rutledge and M. S. Muha, "Imaging antenna arrays," *IEEE Trans. Antennas Propag.*, vol. 30, no. 4, pp. 535–540, 1982.
- [32] C. R. Brewitt-Taylor, D. J. Gunton, and H. D. Rees, "Planar Antennas on a Dielectric Surface," *Electronics Letters*, vol. 17, no. 20, pp. 729–731, 1981.
- [33] S. Maas, *Nonlinear Microwave and RF Circuits*. Artech House, 2003.
- [34] J. Stake, L. Dillner, S. H. Jones, C. Mann, J. Thornton, J. R. Jones, W. L. Bishop, and E. Kollberg, "Effects of self-heating on planar heterostructure barrier varactor diodes," *IEEE Trans. Electron Devices*, vol. 45, no. 11, pp. 2298–2303, Nov. 1998.
- [35] T. Rylander, P. Ingelström, and A. Bondeson, *Computational Electromagnetics*. Springer Science, 2005.
- [36] P. Kuchment, *Floquet Theory for Partial Differential Equations*. Birkhäuser Basel, 2012.
- [37] J. Vukusic, J. Stake, T. Bryllert, Ø. Olsen, and J. Hanning, "Monolithic HBV-Based 282-GHz Tripler With 31-mW Output Power," *IEEE Electron Device Lett.*, vol. 33, no. 6, pp. 800–802, Jun. 2012.
- [38] S. Kazemi, "Design and modelling of 100 GHz HBV quintuplers," Master Thesis, Chalmers University of Technology, 2009.
- [39] W. A. Shiroma, S. C. Bundy, S. Hollung, B. D. Bauernfeind, and Z. B. Popovic, "Cascaded active and passive quasi-optical grids," *IEEE Trans. Microw. Theory Techn.*, vol. 43, no. 12, pp. 2904–2909, Dec. 1995.
- [40] M. A. Morgan and S.-K. Pan, "Graphical Prediction of Trapped Mode Resonances in Sub-mm and THz Waveguide Networks," *IEEE Trans. THz Sci. Technol.*, vol. 3, no. 1, pp. 72–80, 2013.
- [41] A. Al-Zayed, R. R. Swisher, F. Lecuyer, A. C. Guyette, Q. Sun, and M. P. De Lisio, "Reduction of substrate-mode effects in power-combining arrays," *IEEE Trans. Microw. Theory Techn.*, vol. 49, no. 6, pp. 1067–1072, Jun. 2001.
- [42] P. Goldsmith, *Quasioptical Systems: Gaussian Beam Quasioptical Propagation and Applications*. Wiley-IEEE Press, 1997.
- [43] C. Cunningham, "Resonant grids and their use in the construction of submillimetre filters," *Infrared Physics*, vol. 23, no. 4, pp. 207 – 215, 1983.
- [44] A. Y. Tang, E. Schlecht, R. Lin, G. Chattopadhyay, C. Lee, J. Gill, I. Mehdi, and J. Stake, "Electro-thermal model for multi-anode schottky diode multipliers," *IEEE Trans. THz Sci. Technol.*, vol. 2, no. 3, pp. 290–298, May 2012.
- [45] S. A. Rosenau, C. Liang, W. Y. Li, W. K. Zhang, C. W. Domiers, and N. C. J. Luhmann, "Frequency multiplier grid arrays for satellite applications," *International Conference on Infrared and Millimeter Waves*, 2000.

